Journal of Energy Storage 132 (2025) 117902

Contents lists available at ScienceDirect

Journal of Energy Storage

journal homepage: www.elsevier.com/locate/est

Research papers

A multi-objective optimization model for predictive opportunistic maintenance of lithium-ion batteries

Zongyao Wang [a], Wei Shangguan [a,b,*], Zhiqiang Xu [c], Cong Peng [a], Enrico Zio [c,d], Baigen Cai [a,b]

[a] School of Automation and Intelligence, Beijing Jiaotong University, Beijing, 100044, China
[b] State Key Laboratory of Rail Traffic control and safety, Beijing Jiaotong University, Beijing, 100044, China
[c] Energy Department, Politecnico di Milano, Milano, 20156, Italy
[d] MINES Paris-PSL University, CRC, Sophia Antipolis, France

ARTICLE INFO

Keywords:
Lithium-ion battery
Predictive maintenance
Remaining useful life
Evidential regression
Multi-objective optimized maintenance

ABSTRACT

This paper proposes a predictive opportunistic maintenance optimization model for lithium-ion batteries based on remaining useful life (RUL) predictions. First, we introduce a RUL prediction method based on Multi-Head Attention-Temporal Convolutional Networks-Evidential Regression (MA-TCN-ER). The MA-TCN framework captures the global dependencies in multi-dimensional degradation time series of batteries, and evidential regression quantifies the epistemic uncertainty in predictions. Next, the RUL probability density function (PDF) is obtained using kernel density estimation, providing prior knowledge for maintenance decision-making. For individual batteries, we develop a multi-objective maintenance model that considers maintenance cost, availability and reliability measures to determine the optimal preventive replacement time. Based on the optimal replacement time for each component, we calculate the opportunistic maintenance time windows to determine the grouping structure for opportunistic maintenance. The effectiveness of the proposed method is validated using the Oxford lithium-ion battery degradation dataset and the NASA PCoE battery dataset. Experimental results demonstrate that our RUL prediction method provides more accurate RUL estimates than other existing approaches.

1. Introduction

Lithium-ion battery is a kind of energy storage system with the advantages of long life, low environmental pollution and low self-discharge rate [1,2]. It is widely used in the fields of electric vehicles [3], high-speed railway [4,5] and aerospace [6]. However, as the usage time increases, continuous charge and discharge cycles can induce irreversible electrochemical reactions within the lithium-ion battery, leading to capacity degradation and performance deterioration. In some cases, this may lead to accidents posing a risk to personal safety [7].

Prognostics and health management (PHM) by enabling predictive maintenance (PdM) can aid to ensure the reliable operation of lithium-ion batteries and prevent hazardous incidents. This maintenance strategy, integrates remaining useful life (RUL) predictions into maintenance planning for reducing maintenance costs and the frequency of occurrence of failures [8–10].

Within PdM, informed and rational maintenance decisions rely on accurate RUL predictions. RUL refers to the remaining operational time a device can function normally under its current condition, serving as a crucial indicator of its health status or reliability. For lithium-ion batteries, RUL typically represents the time from the present moment until the state of health (SOH) or capacity falls below a predefined threshold [11]. Data-driven approaches have gained popularity in the field of RUL prediction for batteries [12], as they bypass the need for in-depth understanding of the complex physical mechanisms of batteries by learning from monitoring data features [13]. Deep learning has become particularly popular for predicting lithium-ion battery RUL, due to its ability to extract complex and latent features [14]. For instance, Jia et al. [14] proposed a method for predicting the RUL of lithium-ion batteries under small-sample conditions, utilizing convolutional neural networks (CNN) and deep bidirectional long short-term memory networks (DBLSTM). Xie et al. [15] reconstructed the capacity sequence of batteries using complete ensemble empirical mode decomposition with adaptive noise to form prior knowledge; leveraging the prior knowledge, they employed a CNN-LSTM model to achieve real-time RUL prediction for lithium-ion batteries. Similarly, Guo et al. [16] utilized a Savitzky-Golay (SG) filter to denoise the aging features of batteries and subsequently employed a gated recurrent unit (GRU) neural network to predict the RUL of lithium-ion batteries under different charging

* Corresponding author.
E-mail address: wshg@bjtu.edu.cn (W. Shangguan).

https://doi.org/10.1016/j.est.2025.117902
Received 17 January 2025; Received in revised form 1 May 2025; Accepted 26 July 2025
Available online 6 August 2025

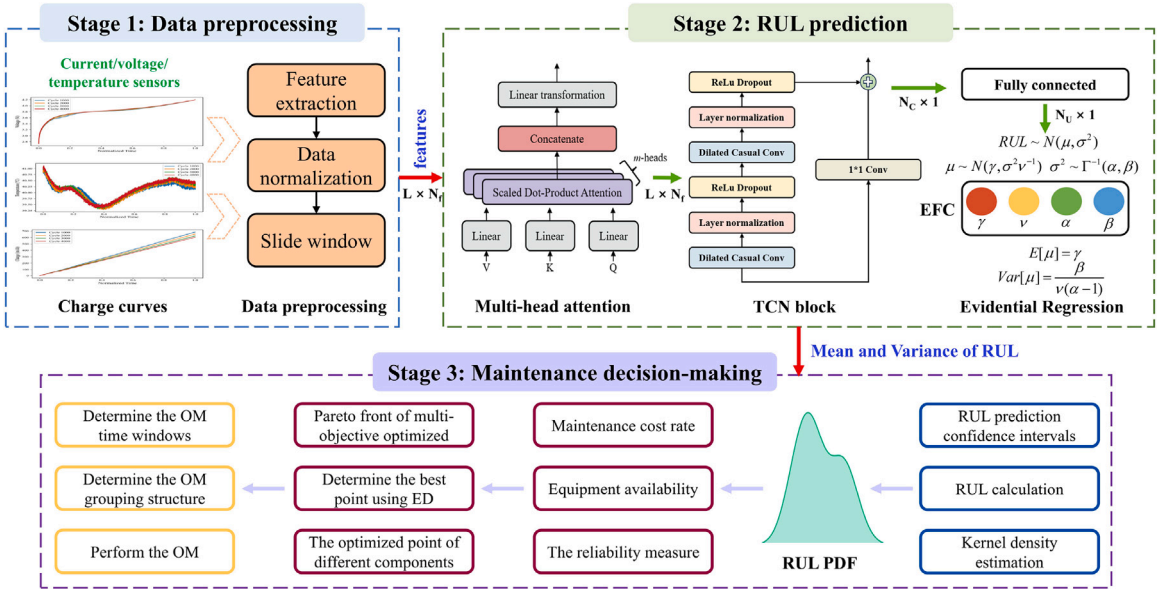

Fig. 1. The framework of the predictive opportunistic maintenance for lithium-ion batteries.

modes; experimental results demonstrated that the root-mean-square error of the predictions could be kept within 1%. The aforementioned RUL prediction methods based on CNN and recurrent neural networks (RNNs) have achieved promising predictive performance but face two major challenges: (1) in multivariate RUL prediction tasks, the internal design of CNNs and RNNs exhibits certain limitations. CNNs have a limited receptive field, requiring the stacking of multiple layers to achieve sufficient coverage [17]. On the other hand, RNNs are prone to information loss and exposed to issues such as vanishing gradients when processing time-series for regression tasks [13]. (2) The aforementioned prediction methods typically focus on developing point-based RUL prediction approaches using neural networks, neglecting predictions uncertainty. However, relying solely on point estimates for maintenance decision-making can lead to suboptimal or even hazardous outcomes [18–20].

Existing maintenance strategies for lithium-ion batteries are predominantly developed under the assumption that battery lifetimes follow specific distributions, with limited research integrating RUL prediction and maintenance decision-making [18]. For example, Jarčević et al. [21] proposed a preventive maintenance strategy involving periodic inspections and scheduled replacements for individual batteries. Wu et al. [22] developed a reinforcement learning-based preventive maintenance method for lithium-ion batteries, leveraging Monte Carlo tree search and deep neural networks to determine optimal maintenance actions. Wang et al. [2] proposed a battery RUL prediction method based on the discharge voltage curve, along with inspection replacement and age-based replacement maintenance strategies; however, these two components are independent of each other. Implementing PdM strategies for lithium-ion batteries enables a comprehensive assessment of their operational status, ensuring safe, reliable and cost-effective system performance. Chen et al. [18] proposed a dynamic, probability-based RUL PdM strategy that effectively reduces maintenance costs. However, most existing PdM research typically focuses only on optimizing maintenance costs. In practice, it is often necessary to also consider the impact of maintenance activities on availability or reliability [23]. Balancing multiple optimization objectives thus becomes an important issue to address. Additionally, most maintenance strategies are designed for single components, making it a challenging task to implement predictive maintenance for multi-component systems.

To address the aforementioned challenges, this paper proposes a predictive opportunistic maintenance strategy for lithium-ion batteries based on Multi-head Attention-Temporal Convolutional Neural Network-Evidential Regression (MA-TCN-ER). First, we introduce a MA-TCN framework that overcomes the limitations of CNNs and RNNs, significantly improving the predictive accuracy of multi-dimensional time-series regression. Second, evidential regression is employed to derive reliable RUL point estimates and the probability density function (PDF) of RUL. Based on probabilistic RUL, we construct a tripartite optimization model for single-component long-term age replacement, integrating considerations of maintenance cost, availability and reliability measures. By optimizing the single-component maintenance model, the optimal replacement time for each battery can be determined, and the opportunistic maintenance (OM) grouping structure can be identified by specifying the OM time window. The main contributions of this study are summarized as follows:

(1) This study proposes an MA-TCN-ER-based battery RUL prediction model, which leverages an attention mechanism to filter out irrelevant information from raw measurements and employs TCN to effectively handle time series regression tasks. Additionally, the use of ER enables both reliable pointwise RUL estimation and probabilistic RUL prediction, providing valuable insights for maintenance strategy formulation.

(2) By considering the maintenance cost, availability and reliability measures of components, a multi-objective optimization model for single-component maintenance decisions is proposed. Building on this model, a predictive opportunistic maintenance strategy for lithium-ion batteries is designed.

(3) Two practical numerical examples illustrate the effectiveness of the proposed predictive opportunistic maintenance strategy.

The remainder of this paper is organized as follows. Section 2 provides an overview of the proposed framework for the predictive opportunistic maintenance strategy. In Section 3, we analyze the implementation process of the probabilistic RUL prediction method based on MA-TCN-ER. Section 4 presents a multi-objective predictive opportunistic maintenance strategy for lithium-ion batteries, leveraging the RUL PDF. In Section 5, the effectiveness of the proposed method is demonstrated using the Oxford lithium-ion battery dataset and the NASA battery dataset. Conclusions and future perspectives are discussed in Section 6.

2. The proposed PdM framework

The proposed framework for predictive opportunistic maintenance of lithium-ion batteries is illustrated in Fig. 1. The framework consists

of three main components: the data preprocessing stage, the RUL prediction stage and the maintenance decision-making stage.

In the data preprocessing stage, features indicative of degradation are extracted based on voltage, temperature and other data collected during the charging phase. The reason for using only the state measurements during the lithium-ion charging process for analysis and RUL prediction is that, compared to the discharge process, the charging process is typically smooth and stable, allowing for easily and accurately measuring the necessary performance parameters of the battery [24, 25]. After normalizing the data, sliding window techniques are applied to generate data samples. The multidimensional data samples are fed into the MA-TCN-ER model to perform RUL prediction.

In the RUL prediction stage, the trained MA-TCN-ER model is employed to output the predicted mean and variance. In Fig. 1, L, N_f, N_C, N_U represent the time steps of the sliding window, the dimensionality of the input features, the number of filters used in the convolutional layers of TCN block, and the number of units in the standard fully connected layers, respectively. EFC denotes the evidential fully connected layer. The proposed neural network model is trained using historical data from lithium-ion batteries, which also undergoes a data preprocessing phase. Unlike the test data, historical data includes both multidimensional features and RUL labels.

After obtaining the predicted mean and variance of the RUL, the RUL estimates under different confidence intervals can be derived. By combining kernel density estimation (KDE) techniques, the functional form of the RUL PDF can be obtained. Considering the probabilistic RUL, the cost rate, availability, and reliability, the optimal maintenance timing for each component is identified. Finally, the opportunity maintenance grouping structure is determined by setting the opportunity maintenance window.

The remaining sections of this paper provide a detailed description of each stage.

3. RUL prediction based on MA-TCN-ER

In this section, we propose a MA-TCN model incorporating evidence regression to predict the RUL of lithium-ion batteries and use KDE to estimate their PDFs.

3.1. MA mechanism

The multi-head attention mechanism was introduced by Vaswani et al. in 2017 [26], which is an extended form of the attention mechanism in deep learning models. Compared to a single attention mechanism, multi-head attention can extract information from different representation subspaces [27]. The use of MA enhances the predictive model's ability to learn diverse feature representations and generate enhanced features, thereby improving the expressiveness of the primary model [28].

MA computes scaled dot-product attention for each attention head. The output for each head is calculated using Eq. (1):

$$H_{(i)} = A(Q_i, K_i, V_i) \tag{1}$$

where Q, K and V represent the query vector, key vector and value vector, respectively. A denotes a single scaled dot-product attention.

The outputs of all attention heads are, then, concatenated, as expressed by the following equation:

$$MHA = Concat(H_1, H_2, \dots, H_m)W^c \tag{2}$$

where m it the number of the heads and W^c is a learnable weight matrix.

The MA mechanism prioritizes the most relevant features for RUL prediction among various inputs (e.g., voltage, current, SOH), effectively filtering out irrelevant information [29].

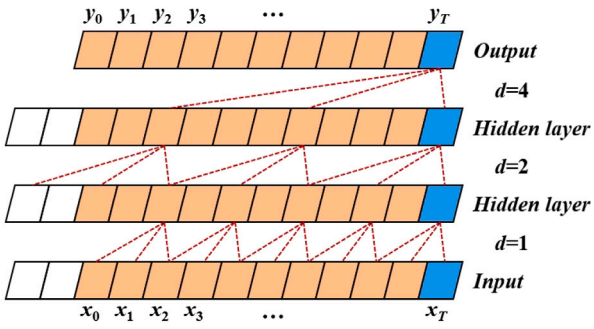

Fig. 2. The structure of causal dilation convolution block.

3.2. TCN block

TCN was proposed by Bai et al. in 2018 [30]. Compared to traditional RNN models such as LSTM or GRU, TCN benefits from causal and dilated convolutions, which help mitigate the issues of gradient vanishing and gradient explosion often encountered in RNNs when dealing with long time sequences. Furthermore, TCNs can adjust the convolutional kernel size and expansion coefficients to obtain a more flexible sensory field. TCN mainly contains two main structures: (a) causal dilation convolution and (b) residual connection.

Suppose that the input sequence $x = (x_0, x_1, x_2, x_3, \dots, x_T)$, and $y = (y_0, y_1, y_2, y_3, \dots, y_T)$ is the output sequence we wish to predict. In the actual prediction process, sequential modeling is an unavoidable problem [31,32]. Considering a certain time point t, the output y_t is usually determined by the sequence $(x_0, x_1, \dots, x_t)$, and the future input sequence $(x_{t+1}, x_{t+2}, \dots, x_T)$ is not utilized. TCNs can efficiently handle sequence modeling tasks and make predictions relevant only to current and historical input sequences. Therefore, the TCN should have a directional structure to prevent information leakage from the past to the future.

To achieve this objective, TCN employs the structure of causal dilated convolution. Causal dilated convolution has the advantage of both causal and dilated convolution and is the core of TCN. The structure of causal dilation convolution is shown in Fig. 2. For a 1-D input sequence $x \in R^n$ and a filter $f : \{0, 1, 2, \dots, k-1\}$, the dilation convolution operation in the input sequence with elements s can be defined as

$$F(s) = (x^* f)(s) = \sum_{i=1}^{D-1} f(i) \cdot x_{s-di} \tag{3}$$

where D is the convolution kernel size, * is the convolution operator and x_{s-di} is the input element for current and historical information; d is the dilation factor, and when $d = 1$, the dilation convolution can be regarded as a regular convolution.

Another important block of TCN is the residual connection. The residual connection block can not only transfer information across layers, but also enhance the generalization capability of TCN. The structure of the residual connection is shown in Fig. 3. It is assumed that x is the input of the residual connection block and $F(x)$ is the transformation; then, the output of the block $H(x)$ can be defined as

$$H(x) = F(x) + x \tag{4}$$

This allows the layers to learn modifications to the identity mapping, which has been repeatedly shown to be beneficial in simplifying the training process and stabilizing the deep networks.

TCN eliminates the recurrent connections used in RNNs, effectively preventing information loss [13]. Additionally, it employs residual connections to mitigate the vanishing gradient problem, making it more suitable for handling complex and long multivariate time-series data from batteries.

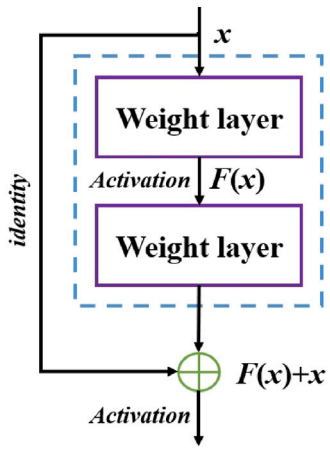

Fig. 3. The structure of residual connection block.

However, using TCN alone for RUL prediction often focuses only on features at a single time scale while overlooking the importance of features at other time scales [13]. To address this, this study integrates MA with TCN, enriching the representation of input sequences and effectively capturing information across multiple time scales. Moreover, the MA mechanism provides global information features, which, when combined with the causal pattern learning capability of the TCN, enhance the performance of the predictive model. Following the TCN layer, a fully connected layer is added to integrate the features extracted from the outputs.

3.3. Uncertainty quantification using evidence regression

After the MA-TCN layer, evidence regression [33] is employed to quantify the epistemic and aleatoric uncertainties of prediction, providing statistical knowledge for estimating the uncertainty in RUL predictions.

The evidence-based neural network uncertainty quantification method directly incorporates prior information into the likelihood function. By training the network to output the hyperparameters of the higher-order evidence distribution, it can learn epistemic and aleatoric uncertainty without the need for sampling [34,35]. Evidence regression models the uncertainty of the regression network by learning the parameters of the evidence distribution.

In this paper, an evidence fully connected layer is added after the basic fully connected layer, followed by the use of an evidence regression loss function, which aims at maximizing the model fit and minimizing evidence on errors.

Gaussian distributions are widely used in many RUL prediction tasks to represent aleatory uncertainties [36–38]. However, minimizing the likelihood function of a conventional Gaussian distribution can only quantify the aleatoric uncertainty arising from the data itself while neglecting the epistemic uncertainty in model predictions [33,39]. ER quantifies both the aleatoric uncertainty inherent in the data and the epistemic uncertainty of the predictive model by placing higher-order prior distributions on the unknown parameters to be estimated. Specifically, ER assigns a Gaussian prior to the unknown mean of the Gaussian distribution and an inverse gamma prior to the unknown variance.

This paper assumes that the predicted RUL y follows a Gaussian distribution with both the mean and variance being unknown:

$$y \sim N(\mu, \sigma^2), \mu \sim N(\gamma, \sigma^2 v^{-1}), \sigma^2 \sim \Gamma^{-1}(\alpha, \beta) \tag{5}$$

where $\Gamma(\cdot)$ is the Gamma function, and $\gamma \in R, v > 0, \alpha > 1, \beta > 0$.

Unlike traditional maximum likelihood estimation, evidential regression employs probabilistic estimation to determine the mean μ and variance σ^2. Specifically, it constructs a Normal-Inverse-Gamma (NIG) prior distribution for μ and σ^2, as expressed in Eq. (6):

$$p(\mu, \sigma^2 \mid \gamma, v, \alpha, \beta) = \frac{\beta^\alpha \sqrt{v}}{\Gamma(\alpha)\sqrt{2\pi\sigma^2}} \left(\frac{1}{\sigma^2}\right)^{\alpha+1} \cdot A \tag{6}$$

where A is $\exp\left\{-\frac{2\beta+v(\gamma-\mu)^2}{2\sigma^2}\right\}$, γ and v are used to control the uncertainty of μ, whereas α and β are used to control the uncertainty of σ^2.

Given the NIG distribution, the predictive uncertainty $E[\mu]$, aleatoric uncertainty $E[\sigma^2]$ and epistemic uncertainty $\mathrm{Var}[\mu]$ can be calculated as follows:

$$E[\mu] = \gamma, E[\sigma^2] = \frac{\beta}{\alpha - 1}, \mathrm{Var}[\mu] = \frac{\beta}{v(\alpha - 1)} \tag{7}$$

Epistemic uncertainty, also known as model uncertainty, refers to the uncertainty in the estimation process of RUL predictions. Therefore, this study focuses exclusively on quantifying epistemic uncertainty.

Before training the model using the evidence regression loss function, the parameters γ, v, α, β of the distribution are first generated using EFC. Specifically, after obtaining the output from the standard fully connected layer in the MA-TCN module, the EFC first constructs a fully connected layer with 4 units and no activation function to generate all the distribution parameters. Then applies the Softplus activation function to ensure the non-negativity of v, α, β. The expression for the Softplus function is given as:

$$\mathrm{Softplus}(x) = \ln(1 + \exp^x) \tag{8}$$

Let $\theta = \{\mu, \sigma^2\}$ and $m = \{\gamma, v, \alpha, \beta\}$. Given the observed RUL y_i, the model evidence (marginal likelihood) can be computed by marginalizing the likelihood parameters θ.

$$\begin{aligned} p(y_i|m) &= \frac{p(y_i|\theta, m)p(\theta|m)}{p(\theta|y_i, m)} \\ &= \int_{\sigma^2=0}^{\infty} \int_{\mu=-\infty}^{\infty} p(y_i|\mu, \sigma^2) p(\mu, \sigma^2|m)\, d\mu\, d\sigma^2 \end{aligned} \tag{9}$$

By placing the NIG evidence prior on the traditional Gaussian likelihood function, the analytical solution of Eq. (9) can be obtained [33]:

$$p(y_i|m) = \mathrm{St}(y_i; \gamma, \frac{\beta(1+v)}{v\alpha}, 2\alpha) \tag{10}$$

where $\mathrm{St}(\cdot)$ is the Student-t distribution.

The negative logarithm of the model evidence is defined as $\mathcal{L}_i^{NLL}(\omega)$, and its expression is as follows:

$$\begin{aligned} \mathcal{L}_i^{NLL}(\omega) = &\frac{1}{2}\log(\frac{\pi}{v}) - \alpha\log(\Omega) + \log(\frac{\Gamma(\alpha)}{\Gamma(\alpha+\frac{1}{2})}) \\ &+ (\alpha + \frac{1}{2})\log((y_i - \gamma)^2 v + \Omega) \end{aligned} \tag{11}$$

where $\Omega = 2\beta(1 + v)$.

By minimizing $\mathcal{L}_i^{NLL}(\omega)$, the model parameters are aligned with the observed RUL, ensuring that the predicted distribution covers the true RUL.

Additionally, in the case of prediction errors, ER mitigates the evidence of uncertain predictions by applying evidence penalties or actively increasing uncertainty. A new evidence regularization loss function is proposed to penalize errors in predictions:

$$\mathcal{L}_i^R(\omega) = |y_i - E[\mu_i]| \cdot (2v + \alpha) \tag{12}$$

The total evidence regression loss is composed of these two loss terms [33]:

$$\mathcal{L}_i(\omega) = \mathcal{L}_i^{NLL}(\omega) + \lambda\mathcal{L}_i^R(\omega) \tag{13}$$

where λ is a regularization coefficient. A lower λ value indicates higher confidence in the model's predictive performance, whereas a higher λ value signifies greater uncertainty in the model's output predictions [33].

3.4. RUL calculation based on KDE

After obtaining the predicted mean RUL and the upper and lower bounds under different confidence intervals, KDE is utilized to estimate the resulting RUL PDF.

Considering epistemic uncertainty, the equation for calculating the upper and lower bounds of the RUL under different confidence intervals is:

$$rul_{CI} = \gamma \pm Z \cdot \sqrt{\frac{\beta}{\nu(\alpha - 1)}} \tag{14}$$

where Z represents the critical value of the standard normal distribution corresponding to the desired confidence level.

The mean RUL prediction, and the upper and lower bound prediction results under different confidence intervals are used to obtain a set of RUL values, denoted as $[rul_1, rul_2, \ldots, rul_N]$.

The predicted PDF of the RUL is estimated using KDE. Its mathematical expression is given as:

$$\hat{f}(rul) = \frac{1}{N\omega} \sum_{i=1}^{N} K\left(\frac{rul - rul_i}{\omega}\right) \tag{15}$$

where ω denotes the bandwidth and K is the most commonly used Gaussian kernel function in this paper.

To ensure smoothness and continuity of the estimated PDF, a rule of thumb is typically applied to determine the optimal bandwidth ω, as suggested in [18,40]. The formula for bandwidth selection is expressed as:

$$\omega = \left(\frac{\int (K(x))^2 dx}{\hat{\sigma_k}^4 \int (\hat{f}''(x))^2 dx}\right)^{\frac{1}{5}} N^{-\frac{1}{5}} \approx 1.06 \hat{\sigma_k} N^{-\frac{1}{5}} \tag{16}$$

where $\hat{\sigma_k}$ is the standard deviation of the predicted RUL values.

4. A predictive opportunistic maintenance strategy for lithium-ion batteries

In this section, we propose a probabilistic RUL-based predictive opportunistic maintenance strategy for lithium-ion batteries. The implementation of this strategy involves two steps. The first step is to determine the optimal maintenance time for individual components. A multi-objective optimization strategy is developed for single devices, considering both maintenance costs and reliability, and the optimal maintenance time is identified using Euclidean distance. The second step is to determine which components can undergo opportunistic maintenance based on the defined maintenance window.

4.1. Multi-objective optimization strategy for individual components

This paper proposes a multi-objective optimization-based PdM strategy for individual components to reduce maintenance costs while extending the service life of the equipment and preventing failures. Based on the practical execution process of maintenance tasks, the maintenance activities in this study are defined as replacement activities. These replacement activities are divided into preventive replacement and post-failure replacement. The cost of preventive replacement is denoted as C_p, the cost of post-failure replacement is denoted as C_f, and the installation cost of the equipment is denoted as S.

Assuming the current time is h, the reliability function of the equipment at this time, based on probabilistic RUL, is expressed as:

$$R(t) = Pr(rul_h \geq t) = 1 - Pr(rul_h \leq t) = 1 - \hat{F}(rul) \tag{17}$$

According to the renewal reward theorem, the maintenance cost rate for a single component is defined as:

$$C(\tau) = \frac{E(\text{cost during one maintenance cycle})}{E(\text{length during one maintenance cycle})} \tag{18}$$

where τ is the variable to be optimized, representing the time interval for preventive replacement occurring at $h + \tau$. A maintenance cycle is defined as the period during which a component undergoes a replacement activity, whether it is predictive replacement or post-failure replacement, marking the conclusion of the cycle.

The expected maintenance cost for a single component is given by:

$$\begin{aligned} E(C(\tau)) &= S + C_p * Pr(rul_h > \tau) + C_f * Pr(rul_h \leq \tau) \\ &= S + C_p * R(\tau) + C_f * (1 - R(\tau)) \end{aligned} \tag{19}$$

The expected operational time for a component over one cycle is:

$$\begin{aligned} E(T(\tau)) &= h + \int_0^{\tau} u d\, Pr(rul_h \leq u) + \tau Pr(rul_h > \tau) \\ &= h + \int_0^{\tau} R(u) du \end{aligned} \tag{20}$$

By combining Eqs. (19) and (20), the maintenance cost rate for a single component can be expressed as:

$$C(\tau) = \frac{S + C_p * R(\tau) + C_f * (1 - R(\tau))}{h + \int_0^{\tau} R(u) du} \tag{21}$$

In addition to the maintenance cost rate, this study considers equipment availability and reliability as attributes of the maintenance decision-making process, thereby defining a triple-objective maintenance decision model.

Assuming the current time is h, the time required for preventive replacement is T_p and the time consumed for replacement after failure is T_f, the definition of equipment availability is [41]:

$$A(\tau) = \left[1 + \frac{T_f(1 - R(\tau)) + T_p R(\tau)}{h + \int_0^{\tau} R(u)\, du}\right]^{-1} \tag{22}$$

The aim of optimized maintenance is to achieve the highest equipment availability, which corresponds to minimizing $\overline{A}(\tau) = 1 - A(\tau)$.

The rest optimization objective considered reflects the remaining operational time and reliability performance of the equipment, defined as:

$$P(\tau) = \tau R(\tau) \tag{23}$$

The aim is for the equipment's remaining operational time τ to be as long as possible while maximizing $R(\tau)$ to the greatest extent feasible, i.e. larger of value of $P(\tau)$.

The multi-objective optimization problem for single-component predictive maintenance is, then, aimed to minimize maintenance cost rate $C(\tau)$, equipment unavailability $\overline{A}(\tau)$ and component unreliability measure $\overline{P}(\tau) = 1 - P(\tau)$. The corresponding mathematical model is as follows:

$$\min_{\tau} = [C(\tau), \overline{A}(\tau), \overline{P}(\tau)]^T, 0 < \tau \leq \hat{rul}_h \tag{24}$$

where $\hat{rul}_h$ is the single-point estimation of the component RUL performed at time h.

By optimizing Eq. (24) using a multi-objective optimization algorithm, the Pareto front of the decision variable τ can be obtained. The Pareto front is the set of points in the parameter space that have non-dominated fitness function values and represents the set of optimal solutions for the maintenance time. To select one optimal maintenance time in the set, the Euclidean distance from the ideal point of each solution x_i on the Pareto front is calculated: denoting the ideal point Z^* and the optimized value of each objective optimized individually in Pareto front as $Z^* = \{f_1^*, f_2^*, f_3^*\}$, the Euclidean distance formula $d(x_i)$ is as follows:

$$d(x_i) = \sqrt{\sum_{k=1}^{3} \left(\frac{f(x_{i,k})}{\sum f(x_{i,k})} - f_k^*\right)^2} \tag{25}$$

where f_k^* is the minimum value of $\frac{f(x_{i,k})}{\sum f(x_{i,k})}$, f_1^* denotes the optimal fitness value of $C(\tau)$, f_2^* is the optimal fitness value of $A(\tau)$, f_3^* is the optimal fitness value of $P(\tau)$, and x_i is one solution of the Pareto front.

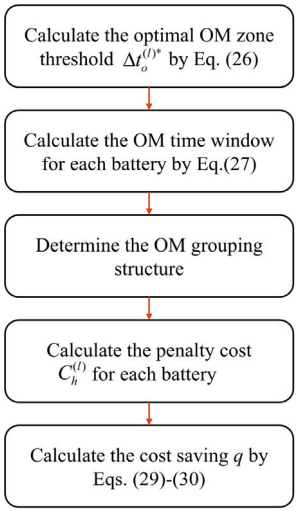

Fig. 4. The execution flow of the proposed OM strategy.

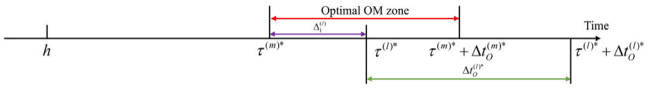

Fig. 5. The OM strategy for the lth component.

After calculating $d(x_i)$ for each solution x_i of the Pareto front, the point closer to the ideal, i.e. with smallest $d(x_i)$, is selected as the optimal preventive replacement time τ^* for the considered component. This provides prior knowledge for scheduling opportunity-based maintenance.

4.2. Opportunistic maintenance strategy

After determining the optimal preventive replacement time for individual components, a predictive opportunity maintenance strategy can be developed. Assume that all the components, i.e. lithium-ion batteries, are of the same type, with same values for C_p, C_f and S. Assume that at time h, there are M lithium-ion batteries operating simultaneously. We want to calculate the opportunity maintenance time window for each lithium-ion battery and determine which components are eligible for opportunity maintenance. The execution flowchart of the proposed OM strategy for multi-component systems is presented in Fig. 4.

Before determining the OM time window, the optimal OM zone threshold $\Delta t_o^{(l)*}$ [42] is, first, defined as shown in Eq. (26):

$$S = c_h^{(l)} \Delta t_o^{(l)*} \tag{26}$$

where $c_h^{(l)}$ is the additional cost rate when the lth component performs OM, representing an inherent attribute of the equipment.

Therefore, based on Eq. (26), the OM time window for the lth lithium-ion battery can be expressed as Eq. (27):

$$OMN_w^{(l)} = [\tau^{(l)*}, \tau^{(l)*} + \Delta t_o^*] \tag{27}$$

It is assumed that the minimum value of different optimal maintenance moments is $\tau^{(m)*}$ and its OM time window is $OMN_w^{(m)}$. For the lth battery, denote $\Delta_1^{(l)} = \tau^{(l)*} - \tau^{(m)*}$. If $\tau^{(l)*}$ falls within $OMN_w^{(m)}$ and $\Delta_1^{(l)} \le \Delta t_o^{(l)*}$, maintenance activities can be implemented for both the lth and mth lithium-ion battery, as shown in Fig. 5.

If the τ^* of the other components do not fall within the OM time window of the mth component, the OM time window of the component with the second smallest τ^* is calculated, and the process continues iteratively. Following this process, the OM grouping structure can be determined.

Assume that within the OM time window $OMN_w^{(m)}$, a total of v ($v \le M$) components undergo OM operations. The penalty cost $C_h^{(l)}$ for the lth component is given in Eq. (28):

$$C_h^{(l)} = c_h^{(l)}(\tau^{(l)*} - \tau^{(m)*}) \tag{28}$$

Then, the cost saving q through OM can be calculated using Eq. (29):

$$q = (v-1)S - \sum_{\eta=1}^{v} C_h^{(\eta)} = (v-1)S - \sum_{\eta=1}^{v} c_h^{(\eta)}(\tau^{(\eta)*} - \tau^{(m)*}) \tag{29}$$

Suppose the $\tau^{(l)*}$ falls within $OMN_w^{(m)}$ and $\Delta_1^{(l)} \le t_o^{(l)*}$, the cost saving q is:

$$q = S - c_h^{(l)}(\tau^{(l)*} - \tau^{(m)*}) = c_h^{(l)}(\Delta t_o^{(l)*} - \Delta_1^{(l)}) \ge 0 \tag{30}$$

If the current operational time h of these components is the same, the global average saving Q is calculated as follows.

$$Q = \frac{q}{t_s^{(k)} + \tau^{(m)*}} = \frac{(v-1)S - \sum_{\eta=1}^{v} c_h^{(\eta)}(\tau^{(\eta)*} - \tau^{(m)*})}{h + \tau^{(m)*}} \tag{31}$$

5. Experiments and results

This study validates the effectiveness of the proposed predictive opportunistic maintenance method through two real-world case studies: the Oxford lithium-ion battery degradation dataset [43,44] and the NASA PCoE battery aging dataset [45].

5.1. Case study 1: Oxford battery dataset

5.1.1. Dataset description and data preprocessing

The Oxford battery degradation dataset includes eight lithium-ion battery cells (Cell1–Cell8) with a nominal capacity of 740 mAh [43,46]. The performance monitoring equipment used is the Bio-Logic MPG-205 battery tester, and the experimental temperature is set to 40 °C. These battery cells underwent repeated charge and discharge cycles, during which current, voltage and temperature data were collected. After every 100 cycles, a C-rate dis/charge is performed to obtain the current available capacity.

(1) Feature extraction.

The Oxford lithium-ion battery degradation dataset contains measurement data for charge and discharge cycles. In this study, features that characterize degradation are extracted solely from the 1-C charging curves of different cycles to predict the RUL. This is because the capacity of the battery at different cycles can be obtained through the charging curve alone. The proposed method remains applicable even when discharge process data are unavailable.

The relationship between voltage, temperature and charge with normalized time during the charging process of Cell 1 at cycle numbers 1000, 2000, 3000, and 4000 is shown in Fig. 6.

As shown in Fig. 6, with an increasing number of charge–discharge cycles, the battery's charge at the end of charging gradually decreases, while the temperature consistently rises, indicating that both measurements exhibit degradation trends. Although the voltage values at the end of charging appear similar across cycles, they are not constant, suggesting that this feature can also contribute to RUL prediction [13]. Furthermore, given the advantage of using mean values in time-series feature extraction [47], in this study, the values of voltage, temperature and charge at the end of the charging process, along with the average values of these variables during the whole charging process, are selected as features for predicting the RUL of the lithium-ion batteries.

In addition, we also calculate the SOH of the lithium-ion batteries, which effectively reflects the decline in battery performance. The expression for the SOH of a battery is given by Eq. (32):

$$SOH_i = \frac{C_i}{C_n} \tag{32}$$

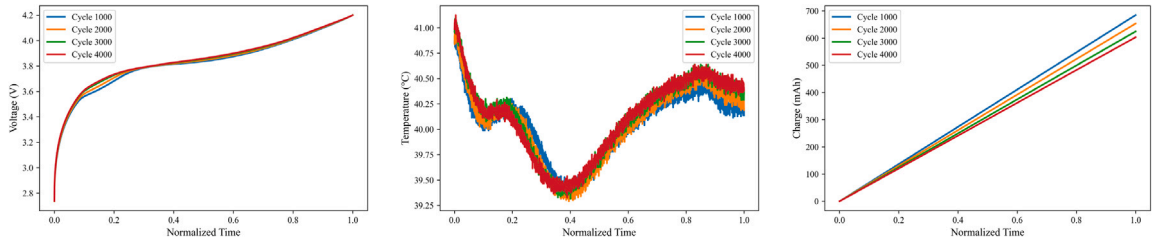

(a) The relationship between voltage with normalized time.

(b) The relationship between temperature with normalized time.

(c) The relationship between charge with normalized time.

Fig. 6. The sensor measurements of different cycles of the charge process.

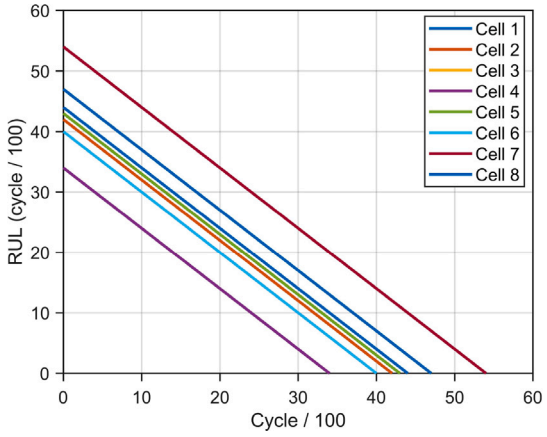

Fig. 7. The RUL labels of various batteries.

where C_i represents the capacity of the battery at the ith cycle, and C_n denotes the nominal capacity. The nominal capacity for Cells 1–8 is 740 mAh. The SOH is also used as input feature to predict the RUL of the batteries.

The RUL labels the of batteries are determined based on the SOH. A battery is considered to have failed when its SOH is less than or equal to 0.8, at which point the RUL label is set to 0. The RUL labels are assigned sequentially according to the cycle order.

The RUL labels for each lithium-ion battery in the Oxford dataset are shown in Fig. 7.

(2) Data normalization.

In this study, the degradation features are scaled to the range $[0, 1]$ using min–max normalization, with the following calculation formula:

$$X_N = \frac{X - \min(X)}{\max(X) - \min(X)} \tag{33}$$

where X_N is the normalized data and X denotes the raw feature data.

(3) Slide window.

In the RUL prediction task, using data from multiple time steps significantly improves prediction accuracy compared to single time-step predictions, as it incorporates more degradation information. Therefore, this study employs a slide window technique to preprocess the lithium-ion battery degradation data [13,48].

5.1.2. Probabilistic RUL prognostics for optimized maintenance strategy development

Each lithium-ion battery in the Oxford degradation dataset includes complete feature measurements from operation to failure. These batteries, all of the same type, are used to validate the proposed PdM strategy. In this study, Cells 1, 3, and 8 are utilized to validate the RUL prediction framework, whereas the degradation measurements of the other batteries serve as historical data to train the MA-TCN-ER model.

To evaluate the performance of the proposed RUL prediction method, this study employs the Root Mean Square Error (RMSE) and Coefficient of Determination R^2 as performance metrics. Their mathematical expressions are as follows:

$$\text{RMSE} = \sqrt{\frac{1}{N}\sum_{i=1}^{N}(rul_i - \hat{rul}_i)^2} \tag{34}$$

$$R^2 = 1 - \frac{\sum_{i=1}^{N}(rul_i - \hat{rul}_i)^2}{\sum_{i=1}^{N}(rul_i - \bar{rul})^2} \tag{35}$$

where rul_i is the true RUL and $\hat{rul}_i$ denotes the predicted RUL of MA-TCN-ER.

In addition, we propose a new metric, the Average Width (AW), to quantify the average width of the prediction interval at a 95% confidence level. Its mathematical expression is given in Eq. (36):

$$\text{AW} = \frac{1}{N}\sum_{i=1}^{N}(U_i - L_i) \tag{36}$$

where U_i is the upper bound of prognostics and L_i is the lower bound of the RUL prediction.

For these evaluation metrics, a smaller RMSE and a larger R^2 indicate better performance in point estimation for RUL prediction; smaller AW value signifies lower prediction uncertainty.

Through a series of testing iterations, the hyperparameter settings for the proposed MA-TCN-ER-driven RUL prediction method are as follows: the number of sliding time windows is set to 10; the number of attention heads in the MA mechanism is 8, and the size of each attention head for query and key is the number of features; the kernel size of the TCN is 4; N_C is 64; the number of units N_U in the FC layer is 10, with the activation function being ReLU; the number of units in the EFC layer is 1; and λ in Eq. (13) is set to 0.001.

All experiments in this study are conducted on a computer equipped with an Nvidia GeForce RTX 4060 GPU. The MA-TCN-ER model is implemented using the TensorFlow 2.15 deep learning framework.

Fig. 8 illustrates the point estimates and 95% confidence intervals of the RUL predictions for Cell 1, Cell 3 and Cell 8 using the MA-TCN-ER model. As shown in Fig. 8, the predicted RUL values for the different lithium-ion batteries are highly consistent with their actual RULs. The predicted intervals almost entirely encompass the true RULs, further validating the effectiveness of the proposed method. Moreover, as the batteries approach their failure time, the confidence intervals become narrower, indicating a gradual reduction in prediction uncertainty.

To further demonstrate the effectiveness of the proposed method, a comparative analysis is conducted using the following models: (1) integration of the MA mechanism with other popular predictive methods, such as MA-LSTM (M1), MA-GRU (M2) and MA-CNN-LSTM (M3); (2) prediction without the MA mechanism, utilizing TCN (M4), LSTM (M5), GRU (M6) and CNN-LSTM (M7) [49], directly. To further illustrate the advantages of the proposed method, we also compare the performance of MA-TCN and the novel dual-stage attention mechanism-based

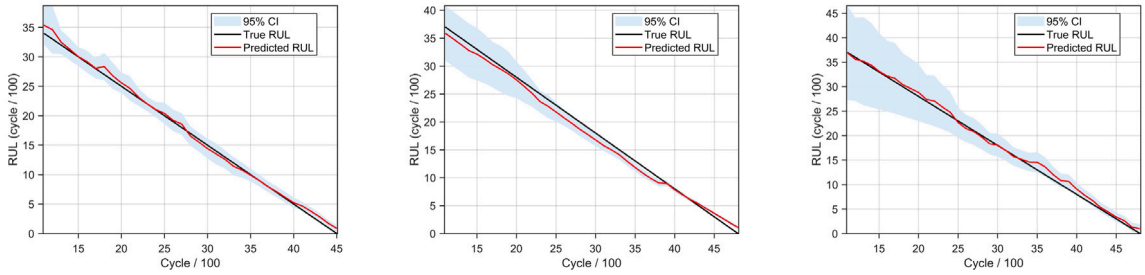

(a) The RUL prediction result of Cell 1. (b) The RUL prediction result of Cell 3. (c) The RUL prediction result of Cell 8.

Fig. 8. The RUL prediction results using MA-TCN-ER.

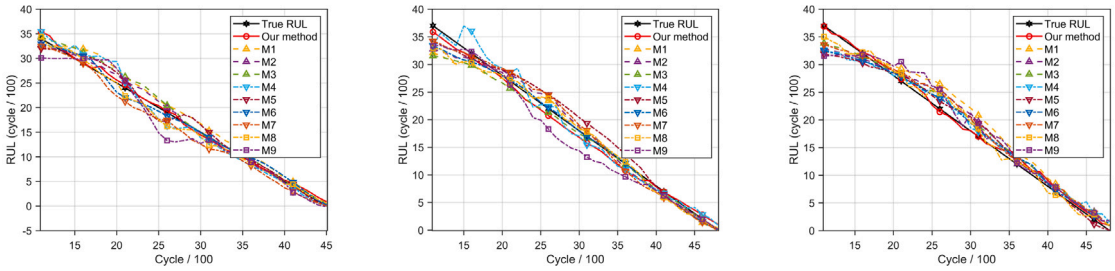

(a) The RUL prediction results of Cell 1 of various methods. (b) The RUL prediction results of Cell 3 of various methods. (c) The RUL prediction results of Cell 8 of various methods.

Fig. 9. The RUL prediction results of various methods.

Table 1
Prediction results of different methods.

Method	RMSE				R^2				AW			
	Cell 1	Cell 3	Cell 8	Mean	Cell 1	Cell 3	Cell 8	Mean	Cell 1	Cell 3	Cell 8	Mean
M1	1.8055	1.7362	2.7142	2.0853	0.9680	0.9749	0.9387	0.9605	13.06	48.40	16.01	25.82
M2	0.8710	1.4750	2.0507	1.4656	0.9926	0.9819	0.9650	0.9798	11.98	748.26	13.54	257.93
M3	1.4436	1.7170	1.5383	1.5663	0.9796	0.9755	0.9803	0.9785	12.48	14.41	12.36	13.08
M4	1.6559	1.5700	1.7392	1.6550	0.9731	0.9795	0.9748	0.9758	2822.00	307.11	18.79	1049.30
M5	1.2902	1.7212	1.8233	1.6116	0.9837	0.9754	0.9724	0.9772	10.49	15.47	12.65	12.87
M6	0.9147	1.1913	1.6364	1.2475	0.9918	0.9882	0.9777	0.9859	10.24	12.63	12.33	11.73
M7	1.6483	1.4147	1.7444	1.6025	0.9734	0.9834	0.9747	0.9772	8.95	14.85	14.73	12.84
M8	1.3727	1.5197	1.0811	1.3245	0.9843	0.9808	0.9885	0.9845	11.02	141.77	78.62	77.14
M9	2.2688	2.3117	2.3400	2.3068	0.9572	0.9556	0.9463	0.9530	13.84	5.24	10.03	9.70
Ours	**0.6164**	**0.9552**	**0.7255**	**0.7657**	**0.9963**	**0.9924**	**0.9956**	**0.9948**	**3.11**	**3.76**	**7.20**	**4.69**

recurrent neural network (DARNN) (M8) [50] with the transformer-based method [51] (M9) for lithium-ion battery RUL prediction. In the transformer-based RUL prediction model, a transformer encoder architecture is utilized, with a time embedding layer [52] added before the Transformer's input to enhance the model's ability to capture complex temporal dependencies. The number of Transformer blocks is set to 3. These predictive methods are combined with the ER framework to enable probabilistic RUL prediction.

Among M1–M9, M4 serves as an ablation study; by comparing the performance of M4 with that of MA-TCN, the effectiveness of the MA mechanism in enhancing RUL prediction can be evaluated. M1–M3 integrate the MA mechanism with commonly used RUL prediction models: LSTM, GRU, and CNN-LSTM, respectively, to demonstrate the advantages of TCN. M5–M7 represent traditional time series prediction models and serve as performance baselines in the comparative analysis. DARNN enhances MA-LSTM by incorporating LSTM units and multi-head attention mechanisms in both its encoder and decoder stages [50,53]. The Transformer model has gained increasing popularity in the field of RUL prediction due to its self-attention mechanism and multi-layer encoder architecture, which excel at capturing complex dependencies [51,52]. Introducing M9 allows for a performance comparison that highlights the capability of MA-TCN in modeling long-term feature dependencies.

The single-point estimation results of different prediction methods are shown in Fig. 9. It is evident that the RUL single-point estimates generated by the proposed method are closer to the actual RUL compared to those produced by other methods. Taking Cell 8 as an example, during the prediction window of 2600 to 3100 cycles, the RUL estimates obtained by other methods are significantly higher than the actual RUL. Performing PdM based on such probabilistic RUL predictions could lead to unexpected equipment failures.

The performance metrics of various prediction methods for different lithium-ion battery prediction tasks are summarized in Table 1. As shown in the Table, for the prediction tasks involving Cell 1, Cell 3 and Cell 8, the proposed MA-TCN achieves the smallest RMSE and AW values and the highest R^2 value, demonstrating the effectiveness and robustness of the proposed method. Taking the prediction task for Cell 3 as an example, the proposed MA-TCN achieves a RMSE value that is 65.86%, 29.23%, 57.30%, 62.78%, 52.22%, 32.61%, 62.60%, 37.15% and 58.68% lower than those of methods M1 through M9.

In the early stages of RUL prediction, some models exhibit high epistemic uncertainty, resulting in significantly higher AW values. This, in turn, reduces the probability density of the RUL PDF at the true RUL value.

Taking the RUL prediction task for Cell 8 as an example, when the current cycle is 2000, the true RUL is 2800 cycles, the widths

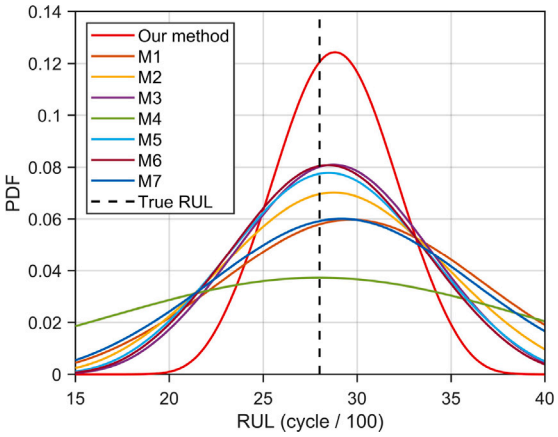

Fig. 10. The RUL PDFs of different methods for Cell 8 when h is 2000 cycles.

of the 95% confidence intervals for these eight methods (ours and M1–M7) are 11.6575, 24.2478, 20.6374, 17.8978, 38.8781, 18.6261, 17.9361, and 24.1159, respectively. Using Eqs. (14)–(16), the RUL PDFs generated by the various methods can be obtained, and are shown in Fig. 10.

As illustrated in Fig. 10, the RUL PDF curves of methods M1 to M7 consistently show probability densities below 0.08 at the true RUL. In contrast, the proposed method achieves a probability density exceeding 0.12 at the true RUL, indicating superior prediction performance. Notably, the probability densities of M3, M5 and M6 at the true RUL are closer to 0.08, because of their narrower 95% confidence interval widths compared to other benchmark methods. Additionally, the RUL PDF curve produced by the proposed method peaks closer to the true RUL than those of the other methods. Furthermore, the proposed method's RUL PDF curve is symmetrically distributed around the true RUL, underscoring its effectiveness.

To demonstrate the advantages of evidential regression in uncertainty quantification, we also compared the performance of the proposed method with that of prediction methods based on the quantile regression loss function (MA-TCN-QLOSS) [18,54]. The expression for the quantile regression loss function is as follows:

$$L_q = q \cdot \max(0, y^{(i)} - \hat{y}_q^{(i)}) + (1-q) \cdot \max(0, \hat{y}_q^{(i)} - y^{(i)}) \tag{37}$$

where $y^{(i)}$ is the true RUL, $\hat{y}^{(i)}$ is the predicted RUL and q is the quantile level.

The structure of the L_q-based prediction method is otherwise consistent with that of MA-TCN-ER, except that the final fully connected layer is replaced with a basic linear fully connected layer, and the loss function is adjusted to Eq. (37). The RUL of all three lithium-ion batteries was predicted using MA-TCN-ER and MA-TCN-QLOSS, with the resulting point estimates of RUL and the predicted 95% confidence intervals shown in Fig. 11. In Fig. 11, the pink dashed line represents the predicted confidence interval of our method, while the blue dashed line indicates the 95% prediction interval obtained using QLOSS.

In terms of point estimation of RUL, except for the mid-stage of the RUL of Cell 3, the point predictions from MA-TCN-ER are closer to the true RUL compared to those from MA-TCN-QLOSS. Additionally, as shown in Fig. 10, the 95% confidence intervals predicted by the proposed method are significantly narrower than those predicted by MA-TCN-QLOSS.

The RMSE of MA-TCN-QLOSS for the RUL predictions of the three batteries are 0.8400, 1.1565, and 4.1188, with R^2 values of 0.9931, 0.9889 and 0.8589, and AW values of 11.16, 8.16 and 9.99, respectively. These performance metrics are all inferior to those of the proposed method. Additionally, MA-TCN-QLOSS requires retraining the model for each quantile prediction, whereas the method proposed in this study only requires training the model once to easily compute estimates for different quantiles, significantly improving training efficiency.

5.1.3. The predictive opportunistic maintenance for lithium-ion batteries

In this section, based on probabilistic RUL, we first determine the optimal replacement time for a single lithium-ion battery using a multi-objective optimization-based single-component maintenance decision model. Subsequently, we identify which components can undergo opportunistic maintenance to reduce maintenance costs by defining an OM time window.

This paper assumes $S = 150$, $C_p = 200$, $C_f = 1000$, $T_p = 1$ cycle and $T_f = 2$ cycles. The ratio of C_f/C_p is 5 [9]. To illustrate the execution process of the proposed multi-objective optimization-based single-component maintenance model, we consider a specific moment in time. Suppose that the current operating cycle of Cell 1, Cell 3 and Cell 8 is 2000 cycles, the relationship between the predicted RUL PDFs and the actual RULs for these three lithium-ion batteries is shown in Fig. 12.

Based on the RUL PDF and Eq. (15), we can obtain the reliability function for each lithium-ion battery, as shown in Fig. 13.

After obtaining the reliability function and incorporating the probabilistic RUL, the Pareto front of the single-component maintenance decision model can be derived by optimizing Eq. (24). A multi-objective genetic algorithm is employed to identify the Pareto front for $C(\tau)$, $\overline{A}(\tau)$ and $\overline{P}(\tau)$. At the prediction time h of 2000 cycles, the Pareto fronts for Cell 1, Cell 3, and Cell 8 are shown in Fig. 14.

To further clarify the trade-offs between different objective functions, the two-dimensional Pareto fronts for $C(\tau)$ and $\overline{A}(\tau)$, $C(\tau)$ and $\overline{P}(\tau)$, as well as $\overline{P}(\tau)$ and $\overline{A}(\tau)$, are presented in Figs. 14–16. As shown in Figs. 15–17, in the multi-objective optimization for different cells, $C(\tau)$ and $\overline{P}(\tau)$ exhibit a conflicting relationship, meaning that improving one fitness function requires sacrificing the other. In contrast, when $\tau \leq 23.4015$, there exists a trade-off between objectives $C(\tau)$ and $\overline{A}(\tau)$, reducing the value of one leads to an increase in the other. Conversely, when $\tau > 23.4015$, both $C(\tau)$ and $\overline{A}(\tau)$ increase together. $\overline{A}(\tau)$ and $\overline{P}(\tau)$

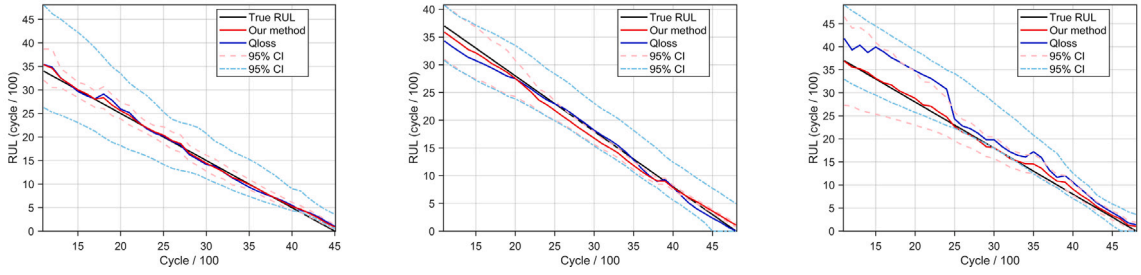

(a) The RUL prediction results of Cell 1. (b) The RUL prediction results of Cell 3. (c) The RUL prediction results of Cell 8.

Fig. 11. The RUL prediction results of MA-TCN-ER and MA-TCN-QLOSS. (For interpretation of the references to color in this figure legend, the reader is referred to the web version of this article.)

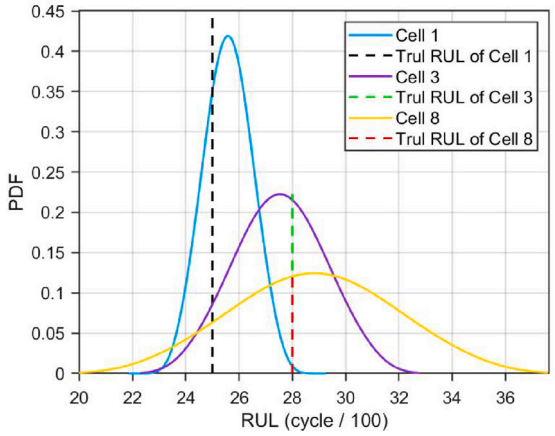

Fig. 12. The RUL PDFs of batteries when h is 2000 cycles.

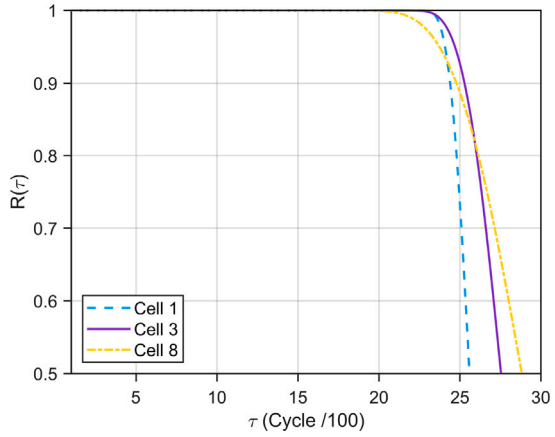

Fig. 13. The reliability functions of batteries when h is 2000 cycles.

exhibit the same trend as well. The Pareto solution set obtained through multi-objective optimization is sorted in ascending order. Taking Cell 1 as an example, the corresponding values of objectives $C(\tau)$, $\overline{A}(\tau)$ and $\overline{P}(\tau)$ for different solutions are shown in Fig. 18. As shown in Fig. 18, the objective values of $C(\tau)$, $\overline{A}(\tau)$ and $\overline{P}(\tau)$ exhibit trends of monotonic increase, decrease followed by increase, and monotonic decrease, respectively. Therefore, for objectives $C(\tau)$ and $\overline{A}(\tau)$, when $\tau \leq 23.4015$, $C(\tau)$ and $\overline{A}(\tau)$ show conflicting trends—one increases while the other decreases. However, when $\tau > 23.4015$, these two objectives follow the same trend, indicating no conflict between them. For objectives $C(\tau)$ and $\overline{P}(\tau)$, their trends are opposing, indicating a fundamental conflict between them. In all other cases, the trends are consistent with the example discussed earlier, which constitutes the underlying cause of the objective conflicts analyzed in this study. Under this condition, when considering all three optimization objectives, the actual optimization problem reduces to a trade-off between $C(\tau)$ and $\overline{P}(\tau)$ under the constraint that $\overline{A}(\tau)$ is at its optimal value. That is, once $\overline{A}(\tau)$ is fixed at its optimal level, a further balance must be struck between $C(\tau)$ and $\overline{P}(\tau)$.

Additionally, taking Cell 1 as an example, the points on the Pareto solution set and their corresponding objective function values are presented in Table 2. As shown in Table 2, $C(\tau)$ and $\overline{P}(\tau)$ exhibit a conflicting relationship, meaning they cannot simultaneously attain their minimum values. For instance, when comparing the 5th and 6th solutions on the Pareto frontier, the 6th solution has a lower maintenance cost rate than the 5th solution, but its corresponding $\overline{P}(\tau)$ value is higher than that of the 5th solution. According to the table, for

Table 2
Comparison results of maintenance optimization for Cell 1.

ID	x_i	$C(\tau)$	$\overline{A}(\tau)$	$\overline{P}(\tau)$	$d(x_i)$
1	23.40	8.16	0.00023156	−22.28	0.0003530
2	23.59	8.23	0.00023194	−22.32	0.0007888
3	23.20	8.14	0.00023190	−22.15	8.1100e−05
4	23.20	8.14	0.00023190	−22.15	8.1100e−05
5	23.32	8.15	0.00023162	−22.24	0.0002203
6	23.21	8.14	0.00023185	−22.16	7.6300e−05
7	23.49	8.19	0.00023164	−22.31	0.0005292
8	23.59	8.23	0.00023194	−22.32	0.0007888
9	23.26	8.14	0.00023173	−22.20	0.0001247
10	23.23	8.14	0.00023181	−22.18	8.4200e−05
11	23.52	8.20	0.00023171	−22.32	0.0005922
12	23.46	8.18	0.00023160	−22.30	0.0004673
13	23.57	8.22	0.00023187	−22.32	0.0007313
14	23.48	8.19	0.00023163	−22.31	0.0005075
15	23.29	8.14	0.00023167	−22.21	0.0001627
16	23.26	8.14	0.00023172	−22.20	0.0001280
17	23.53	8.21	0.00023175	−22.33	0.0006297
18	23.33	8.15	0.00023160	−22.24	0.0002347

Cell 1, when the prediction time is at 2000 cycles, x_6 is selected as the optimal τ since it yields the smallest $d(x)$.

To further investigate the trade-offs among multiple optimization objectives, we conduct a sensitivity analysis on the parameters of the maintenance model. Keeping S, T_p, and T_f constant, we gradually increase the ratio C_f/C_p from 1 to 10. Taking $C(\tau)$ and $\overline{A}(\tau)$ as an example, their two-dimensional Pareto front under different values of C_f/C_p for Cell 1 is shown in Fig. 19. As shown in Fig. 19, $C(\tau)$ and $\overline{A}(\tau)$ are conflicting when C_f/C_p is 1 or 2. However, when $C_f/C_p \geq 3$, $C(\tau)$ and $\overline{A}(\tau)$ exhibit conflicting behavior only at certain time points. This indicates that, with other parameters remaining unchanged, the conflict between $C(\tau)$ and $\overline{A}(\tau)$ weakens as the value of C_f/C_p increases.

When $C_f/C_p = 1$, objectives $C(\tau)$ and $\overline{A}(\tau)$ are in complete conflict, as illustrated by their respective single-objective functions in Fig. 20. In this case, the trends of the single-objective functions for $C(\tau)$ and $\overline{A}(\tau)$ are directly opposing, indicating that the resulting two-dimensional Pareto front between these objectives is conflicting.

Using Eq. (23), the optimal preventive replacement time τ^* for a single lithium-ion battery is determined from the solution set on the Pareto frontier. For Cell 1, Cell 3 and Cell 8 at 2000 cycles, the τ^* are 2319.65 cycles, 2335.62 cycles and 2198.73 cycles, respectively. At the current time, their actual RULs are 2500 cycles, 2800 cycles and 2800 cycles, respectively. This indicates that the optimal replacement times suggested by the multi-objective optimization approach are all slightly lower than the actual RULs, demonstrating the effectiveness of the proposed method.

To further illustrate the effectiveness of the proposed method, Fig. 21 presents the distribution of the actual RULs, single-point RUL estimates, and the τ^* suggested by the multi-objective optimization strategy for different lithium-ion batteries at various prediction time points.

For all three lithium-ion batteries, the τ^* exhibits a similar decreasing trend to the single-point estimates of RUL. As shown in Fig. 21, across the three single-component maintenance decisions, only the recommended τ^* for Cell 3 slightly exceeds the actual RUL at the prediction start points of 4500, 4600 and 4700 cycles. In all other cases, the τ^* is positioned prior to the actual failure time, demonstrating that the proposed method effectively prevents equipment failures.

After determining the optimal scheduled replacement time for each component, we can identify the components eligible for OM by defining the OM time window.

The execution process of the proposed OM strategy can now be illustrated using two examples. One example assumes that all components are simultaneously put into operation, whereas the other example considers multiple components with different current times h.

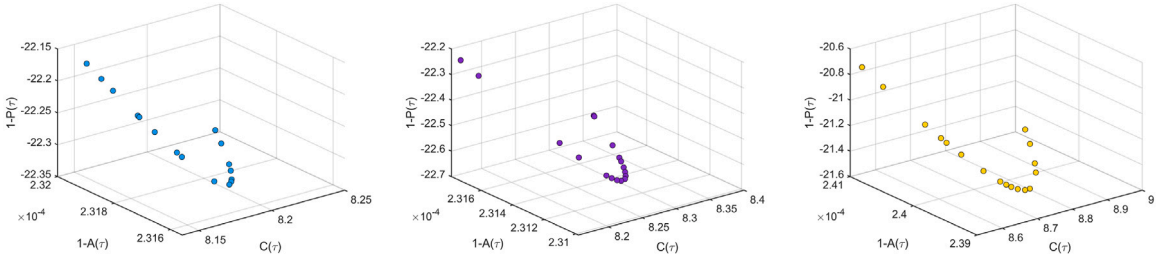

(a) The Pareto front of Cell 1. (b) The Pareto front of Cell 3. (c) The Pareto front of Cell 8.

Fig. 14. The Pareto front of different batteries when h is 2000 cycles.

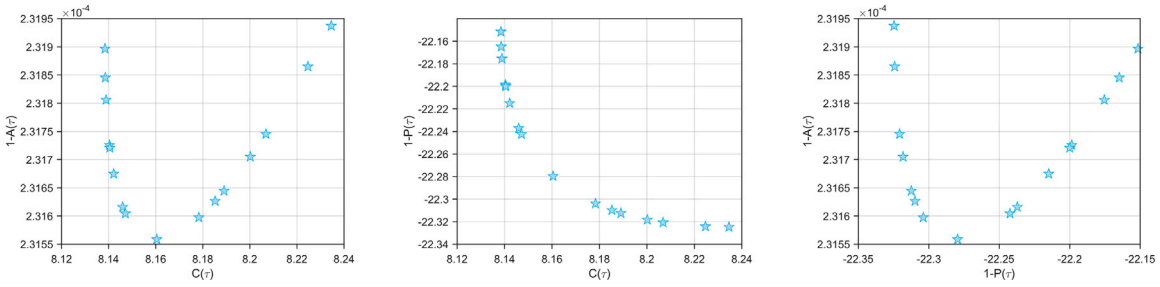

(a) $C(\tau)$ and $\overline{A}(\tau)$. (b) $C(\tau)$ and $\overline{P}(\tau)$. (c) $\overline{P}(\tau)$ and $\overline{A}(\tau)$.

Fig. 15. The two-dimensional Pareto front for Cell 1 when h is 2000 cycles.

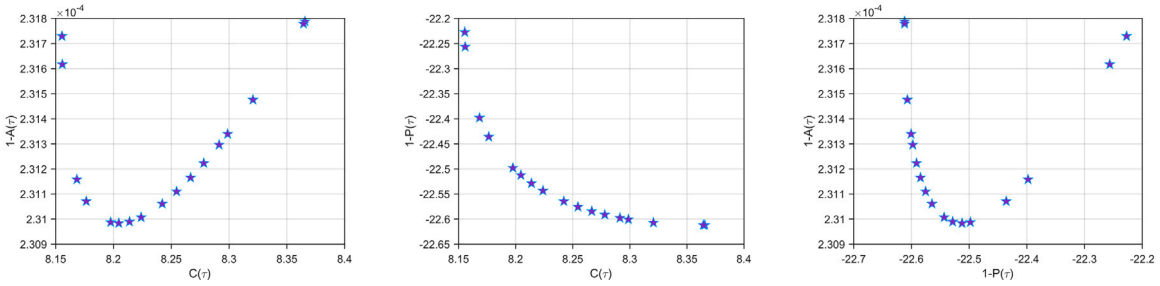

(a) $C(\tau)$ and $\overline{A}(\tau)$. (b) $C(\tau)$ and $\overline{P}(\tau)$. (c) $\overline{P}(\tau)$ and $\overline{A}(\tau)$.

Fig. 16. The two-dimensional Pareto front for Cell 3 when h is 2000 cycles.

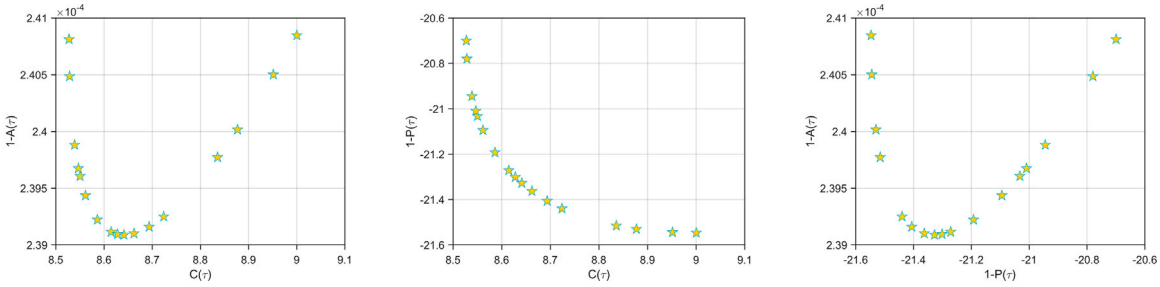

(a) $C(\tau)$ and $\overline{A}(\tau)$. (b) $C(\tau)$ and $\overline{P}(\tau)$. (c) $\overline{P}(\tau)$ and $\overline{A}(\tau)$.

Fig. 17. The two-dimensional Pareto front for Cell 8 when h is 2000 cycles.

Assuming $h = 3000$ cycles, the predicted RULs of Cell 1, Cell 3 and Cell 8 are 1443, 1678 and 1808 cycles, respectively. Their optimal planned preventive replacement times are 1209.17, 1513.02, and 1490.79 cycles. Suppose the additional cost rates $c_h^{(l)}$ for these three batteries are 0.2, 0.1 and 0.15, respectively. The unit of the $c_h^{(l)}$ is the ratio of cost and one cycle.

At this point, the OM windows for these lithium-ion batteries are $[1209.17, 1209.17+750]$, $[1513.02, 1513.02+1500]$ and $[1490.79, 1490.79+1000]$. It is clear that both the τ^* of Cell 3 and Cell 8 fall within the optimal OM window for Cell 1. Moreover, for Cell 3 and Cell 8, their Δ_1 values are both smaller than their Δt_o Therefore, when $h = 3000$

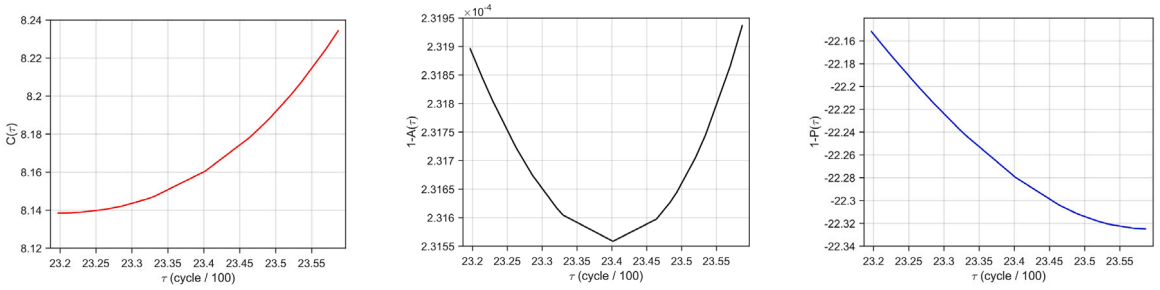

(a) $C(\tau)$. (b) $\overline{A}(\tau)$. (c) $\overline{P}(\tau)$.

Fig. 18. The single-objective values of Pareto solution for Cell 1.

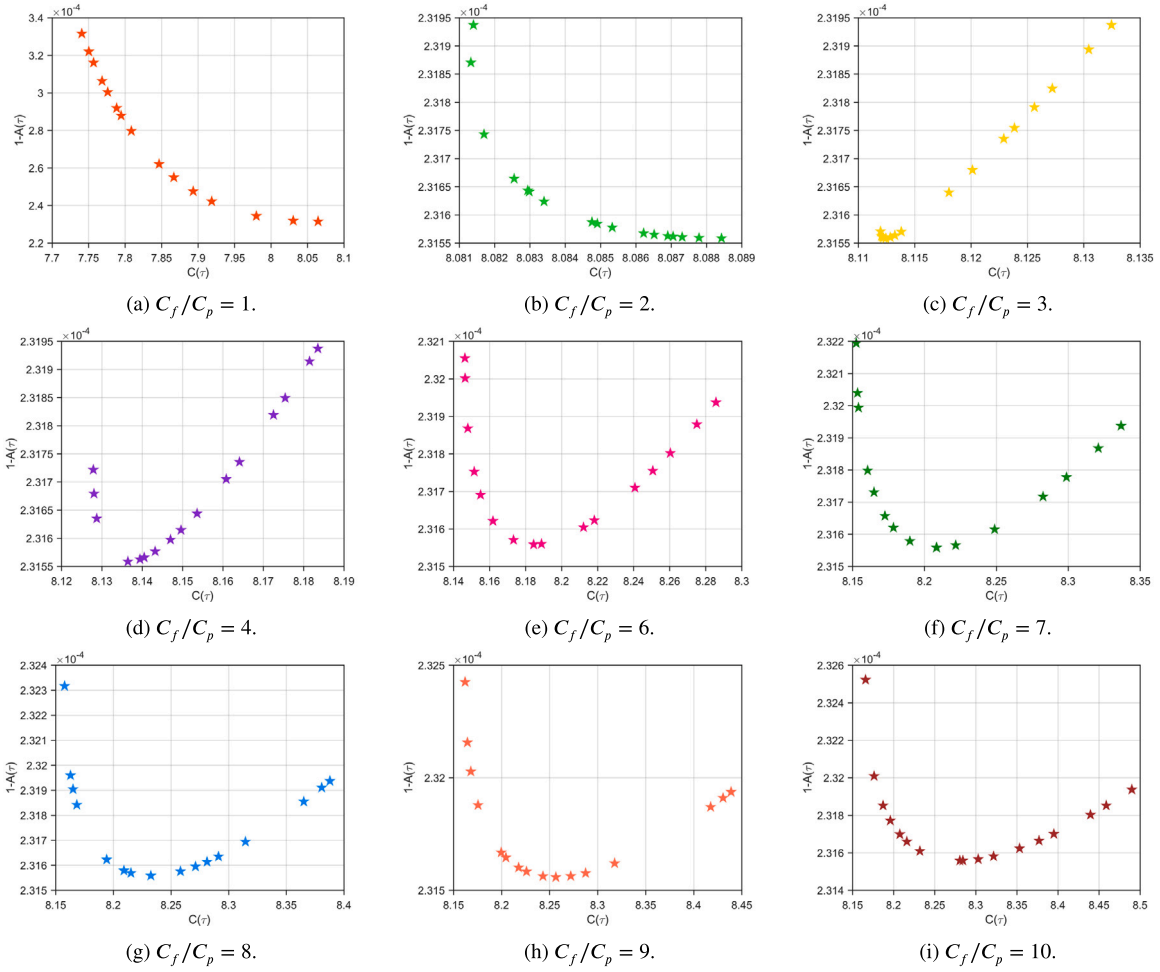

(a) $C_f/C_p = 1$. (b) $C_f/C_p = 2$. (c) $C_f/C_p = 3$.

(d) $C_f/C_p = 4$. (e) $C_f/C_p = 6$. (f) $C_f/C_p = 7$.

(g) $C_f/C_p = 8$. (h) $C_f/C_p = 9$. (i) $C_f/C_p = 10$.

Fig. 19. Two-dimensional Pareto frontiers of $C(\tau)$ and $\overline{A}(\tau)$ in different C_f/C_p for Cell 1.

cycles, all three batteries can undergo OM. The cost saving q_1 is

$$q_1 = 2S - \sum_{\eta=1}^{3} c_h^{(\eta)}(\tau^{(\eta)*} - 12.0917) = 227.3720 \tag{38}$$

The average saving Q_1 is

$$Q_1 = \frac{q_1}{30 + 12.0917} = 5.4018 \tag{39}$$

where the unit of Q_1 is per 100 cycles.

Next, consider another scenario where Cell 1 has run for 3000 cycles, Cell 3 has run for 3500 cycles and Cell 8 has run for 4000 cycles. In this case, the predicted RUL of these three batteries are 1443 cycles, 1184 cycles and 908 cycles, respectively, with the optimal replacement times τ^* being 1209.17 cycles, 1071.27 cycles and 725.71 cycles respectively.

Due to the small RUL loss of Cell 8, the width of its OM time window is quite large. The OM time window for Cell 8 is $[727.51, 727.51 + 1000]$, and it is clear that the τ^* values for Cell 1 and Cell 3 fall within this time window as well. Additionally, for Cell 1 and Cell 3, their Δ_1 values are both smaller than their Δt_o values. Therefore, these batteries can also perform OM. Hence, the cost saving q_2 is

$$q_2 = 2S - \sum_{\eta=1}^{3} c_h^{(\eta)}(\tau^{(\eta)*} - 7.2751) = 298.6875 \tag{40}$$

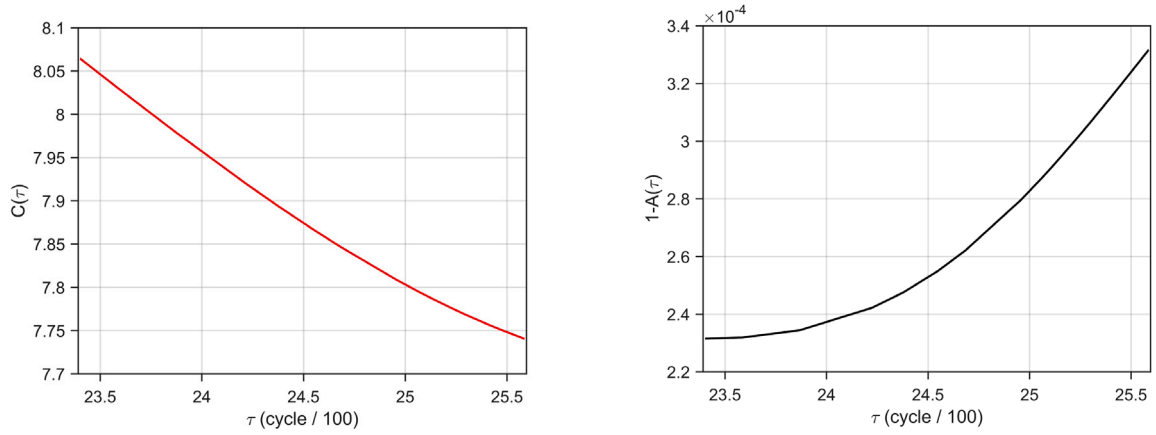

(a) $C(\tau)$. (b) $\overline{A}(\tau)$.

Fig. 20. The single-objective functions of $C(\tau)$ and $\overline{A}(\tau)$ for Cell 1 when $C_f/C_p = 1$.

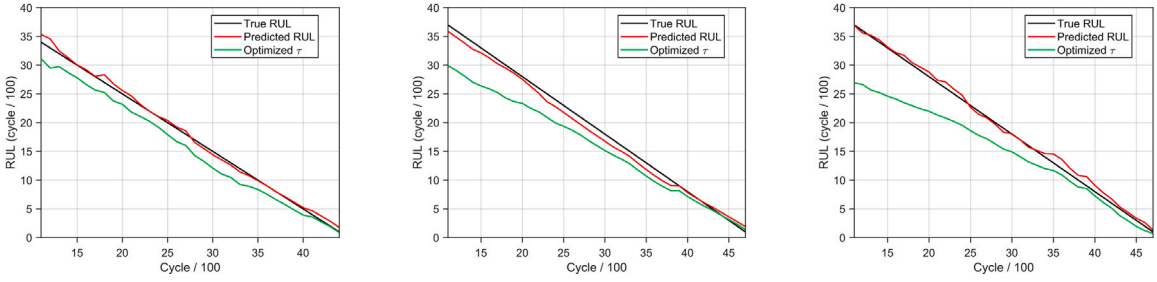

(a) The τ^* of Cell 1. (b) The τ^* of Cell 3. (c) The τ^* of Cell 8.

Fig. 21. The τ^* of different batteries in various prediction starting time.

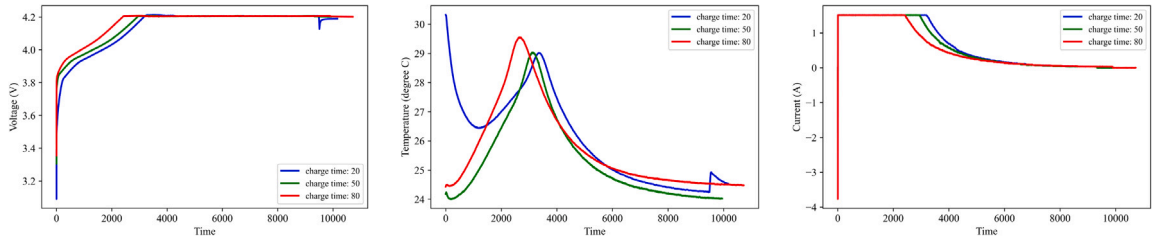

(a) The relationship between voltage with cycles. (b) The relationship between temperature with cycles. (c) The relationship between current with cycles.

Fig. 22. The sensor measurements of different cycles of the charge process for B0005.

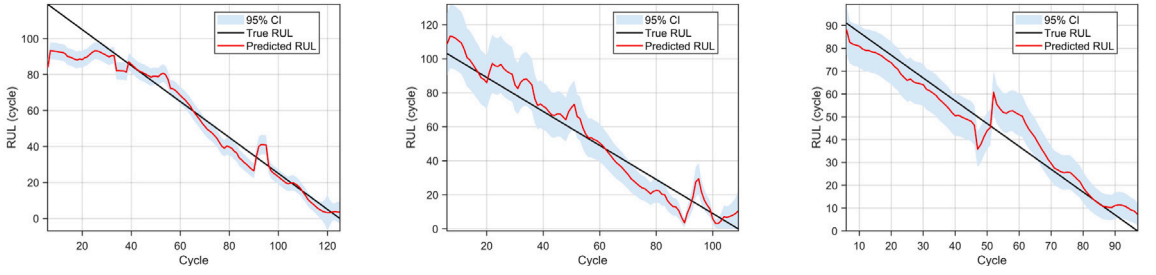

(a) The RUL prediction result of B0005. (b) The RUL prediction result of B0006. (c) The RUL prediction result of B0018.

Fig. 23. The RUL prediction results using MA-TCN-ER for NASA batteries.

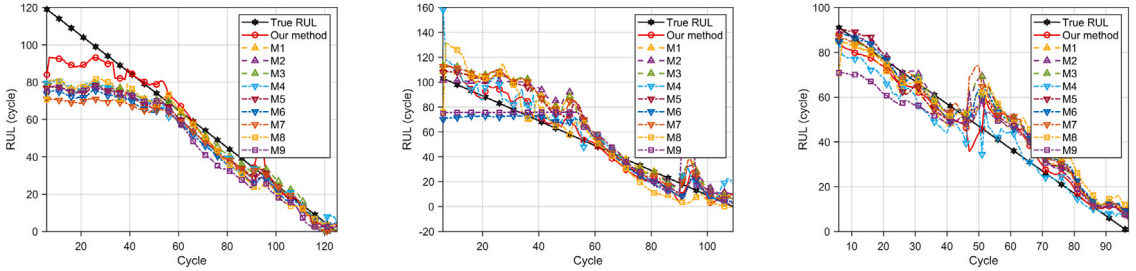

(a) The RUL prediction results of B0005. (b) The RUL prediction results of B0006. (c) The RUL prediction results of B0018.

Fig. 24. The RUL prediction results of various methods for NASA batteries.

Table 3
Prediction results of different methods for NASA batteries.

Method	RMSE				R^2				AW			
	B0005	B0006	B0018	Mean	B0005	B0006	B0018	Mean	B0005	B0006	B0018	Mean
M1	15.3031	15.1255	7.1918	12.5401	0.8048	0.7462	0.9267	0.8259	49.31	45.94	42.36	45.87
M2	15.0739	14.7951	8.5787	12.8159	0.8106	0.7571	0.8956	0.8211	38.74	53.06	60.91	50.90
M3	14.6596	15.0189	8.3161	12.6649	0.8209	0.7497	0.9019	0.8242	45.03	66.83	54.06	55.31
M4	14.8583	11.1241	7.0357	11.0060	0.8160	0.8627	0.9298	0.8695	51.18	207.37	20.55	93.03
M5	15.7464	13.2407	7.0664	12.0178	0.7934	0.8051	0.9292	0.8426	236.54	49.89	45.06	110.50
M6	17.4646	11.6635	7.7384	12.2888	0.7458	0.8491	0.9151	0.8367	35.09	143.36	36.50	71.65
M7	18.9494	15.0357	8.1719	14.0523	0.7008	0.7492	0.8884	0.7795	41.76	44.38	32.75	39.63
M8	14.7178	14.0821	9.3221	12.7073	0.8195	0.7800	0.8768	0.8254	3275.42	2740.70	3683.34	3233.15
M9	16.7700	15.1811	10.0646	14.0052	0.7656	0.7443	0.8564	0.7888	36.28	63.71	36.90	45.63
Ours	**9.1899**	**7.7274**	**6.5762**	**7.8317**	**0.9296**	**0.9337**	**0.9387**	**0.9340**	**9.51**	**22.55**	**16.37**	**16.14**

In this case, because the operating times of each component in the multi-component system are not equal, only the cost saving q can be calculated, and the cost saving rate Q cannot be computed.

In summary, the OM strategy proposed for lithium-ion batteries in this paper not only identifies the optimal preventive replacement time for each component but also helps save maintenance costs through opportunistic maintenance.

5.2. Case study 2: NASA battery dataset

NASA Ames PCoE Research Center conducted charge–discharge experiments on 18 650 lithium-ion batteries (with a rated capacity of 2 Ah) at room temperature and collected various performance metrics using a test bench. In order to further validate the effectiveness of the proposed predictive opportunistic maintenance strategy, we select batteries B0005, B0006, and B0018 from the dataset.

The NASA lithium-ion battery is considered to have failed when its SOH falls to 0.7 or below [55]. Given the limited degradation data in the NASA battery degradation dataset, we assume that the historical measurements of the other two batteries are available when predicting the RUL of a single battery. Taking B0005 as an example, the current, voltage, and temperature curves during the charging process at different cycles are shown in Fig. 22.

As shown in Fig. 22, for NASA lithium-ion batteries, both the total charging time [56] and the time for the current to drop to 0.5 A decrease as the cycle count increases. Therefore, we select these two parameters as features of the charging process. Along with the battery's SOH, these two degradation indicators are used as inputs to the MA-TCN-ER model to accurately predict the RUL of the device.

Setting the sliding time window L is 5, all other parameters of the RUL prediction model remain consistent with the MA-TCN-ER in Case study 1. The probabilistic RUL predictions for B0005, B0006, and B0018 obtained using the proposed method are shown in Fig. 23. As shown in Fig. 23, for the NASA lithium-ion battery dataset, the proposed method accurately captures the trend of the true RUL, with the predicted 95% confidence interval effectively covering the actual RUL. The point estimates of the proposed RUL prediction method, along with those of methods M1–M9, are presented in Fig. 24.

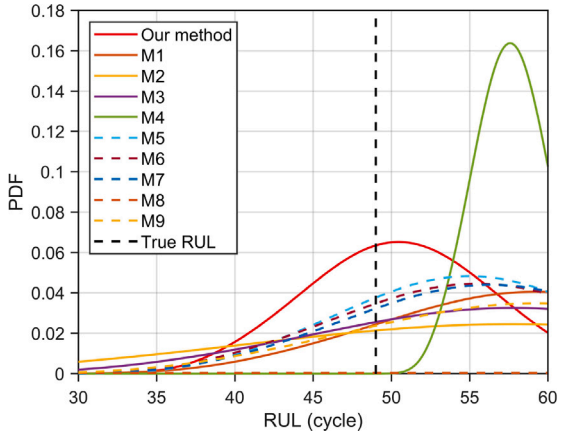

Fig. 25. The RUL PDFs of different methods for B0006 when h is 60 cycles.

As shown in Fig. 24, MA-TCN-ER consistently achieves the highest accuracy across different prediction tasks. Compared to other prediction methods, the proposed approach yields more stable point estimates of RUL, which fluctuate closely around the true RUL. The predictive performance of different forecasting methods is presented in Table 3. It is evident that across various prediction tasks, the proposed MA-TCN-ER consistently achieves the lowest RMSE and AW, as well as the highest R^2. This demonstrates that our RUL estimation method not only provides accurate remaining useful life predictions but also effectively quantifies predictive uncertainty.

Taking B0006 as an example, when the prediction starting point is set to 60 cycles, the relationship between the RUL PDFs estimated by different methods using KDE and the true RUL is shown in Fig. 25.

As shown in Fig. 25, only the proposed method achieves a probability exceeding 0.06 at the true RUL, while all other methods remain below 0.04. The probabilities of TCN and DARNN at the true RUL approach zero, which is attributed to the high uncertainty in these models.

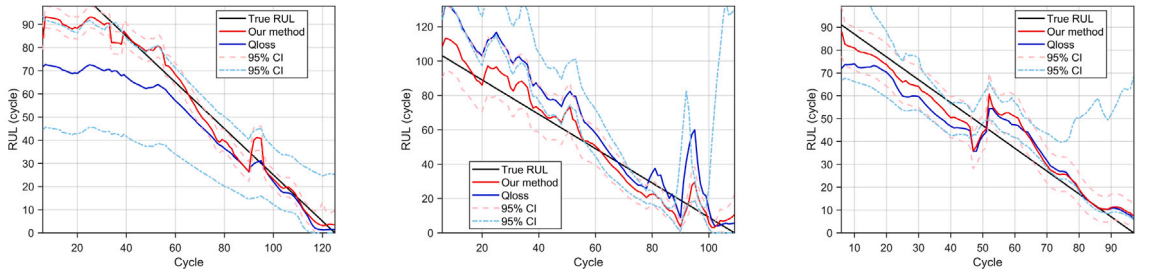

(a) The RUL prediction results of B0005. (b) The RUL prediction results of B0006. (c) The RUL prediction results of B0018.

Fig. 26. The RUL prediction results of MA-TCN-ER and MA-TCN-QLOSS for NASA batteries.

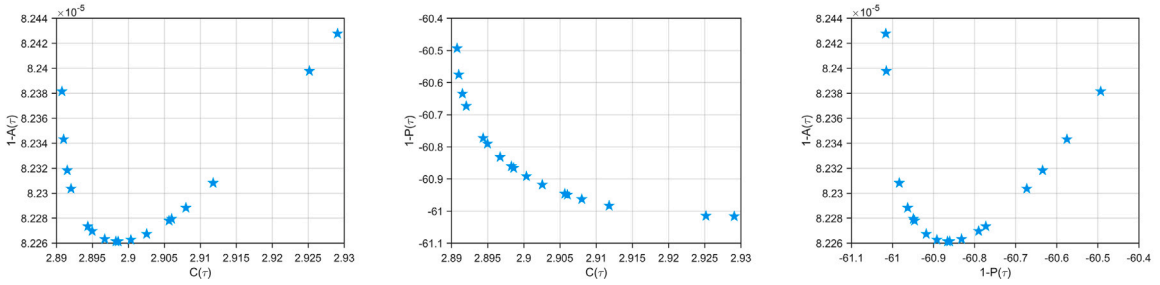

(a) $C(\tau)$ and $\overline{A}(\tau)$. (b) $C(\tau)$ and $\overline{P}(\tau)$. (c) $\overline{P}(\tau)$ and $\overline{A}(\tau)$.

Fig. 27. The two-dimensional Pareto front for B0005 when h is 60 cycles.

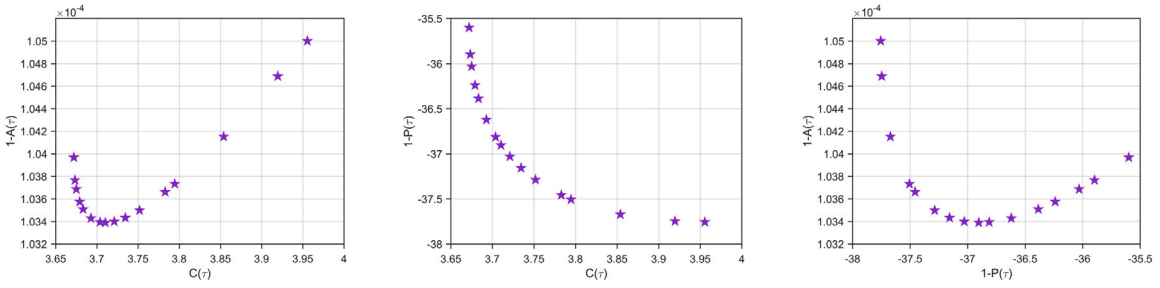

(a) $C(\tau)$ and $\overline{A}(\tau)$. (b) $C(\tau)$ and $\overline{P}(\tau)$. (c) $\overline{P}(\tau)$ and $\overline{A}(\tau)$.

Fig. 28. The two-dimensional Pareto front for B0006 when h is 60 cycles.

To demonstrate the effectiveness of the proposed uncertainty quantification method, we compare the prediction results of MA-TCN using QLOSS with those of MA-TCN-ER, as shown in Fig. 26.

As shown in Fig. 26, compared to MA-TCN-ER, the RUL predictions obtained using MA-TCN-QLOSS exhibit greater deviation from the true RUL, and the width of the predicted 95% confidence interval is significantly wider than that of the proposed method. Furthermore, traditional QLOSS does not impose constraints on the upper and lower bounds of the predicted confidence interval, which may result in point estimates falling outside the confidence interval, as illustrated in Fig. 26(b)–(c).

After obtaining the probabilistic RUL, we first determine the optimal τ^* for each lithium-ion battery through multi-objective optimization. The maintenance model parameters are set consistently with those in Case Study 1. Taking $h = 60$ cycles as an example, the two-dimensional Pareto frontiers among the multiple objectives for B0005, B0006, and B0018 are shown in Figs. 27–29. The results exhibit the same trend as in Case Study 1, indicating that only $C(\tau)$ and $\overline{P}(\tau)$ are in conflict, whereas both $C(\tau)$ and $\overline{A}(\tau)$, as well as $\overline{P}(\tau)$ and $\overline{A}(\tau)$ can exhibit conflicting behavior only at certain time points.

In Case Study 2, we also conducted a sensitivity analysis of parameter C_f/C_p. Taking B0006 as an example, when $h = 60$ cycles, the Pareto frontiers of $C(\tau)$ and $\overline{A}(\tau)$ under different values of C_f/C_p are shown in Fig. 30. As shown in Fig. 30, the conflict between $C(\tau)$ and $\overline{A}(\tau)$ decreases as C_f/C_p increases, which is consistent with the conclusions drawn from the Oxford dataset.

After obtaining the probabilistic RUL, the optimal τ^* for each battery is determined through multi-objective optimization, as shown in Fig. 28. As shown in Fig. 31, almost all values of τ^* are below the actual RUL, further validating the effectiveness of the proposed PdM strategy.

When $h = 60$ cycles, the $c_h^{(l)}$ values for B0005, B0006, and B0018 are 20, 15, and 10, respectively. The unit of the $c_h^{(l)}$ is the ratio of cost and one cycle. Their corresponding OM time window widths are 7.5, 10, and 15. In this case, OM can be performed on B0006 and B0018, yielding values of $q_3 = 140.4632$ and $Q_3 = q_3/(60 + 36.8585) = 1.4502$.

6. Conclusions

This paper presents a predictive opportunistic maintenance strategy for lithium-ion batteries, which leverages probabilistic RUL predictions and incorporates multi-objective, opportunistic maintenance decision-making to achieve effective long-term maintenance planning.

In terms of RUL prediction, the proposed MA-TCN-ER model demonstrates superior single-point RUL estimation accuracy and more precise

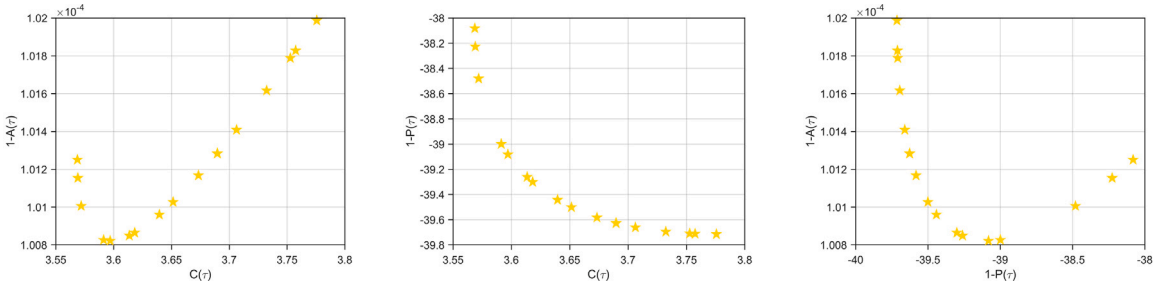

(a) $C(\tau)$ and $\overline{A}(\tau)$. (b) $C(\tau)$ and $\overline{P}(\tau)$. (c) $\overline{P}(\tau)$ and $\overline{A}(\tau)$.

Fig. 29. The two-dimensional Pareto front for B0018 when h is 60 cycles.

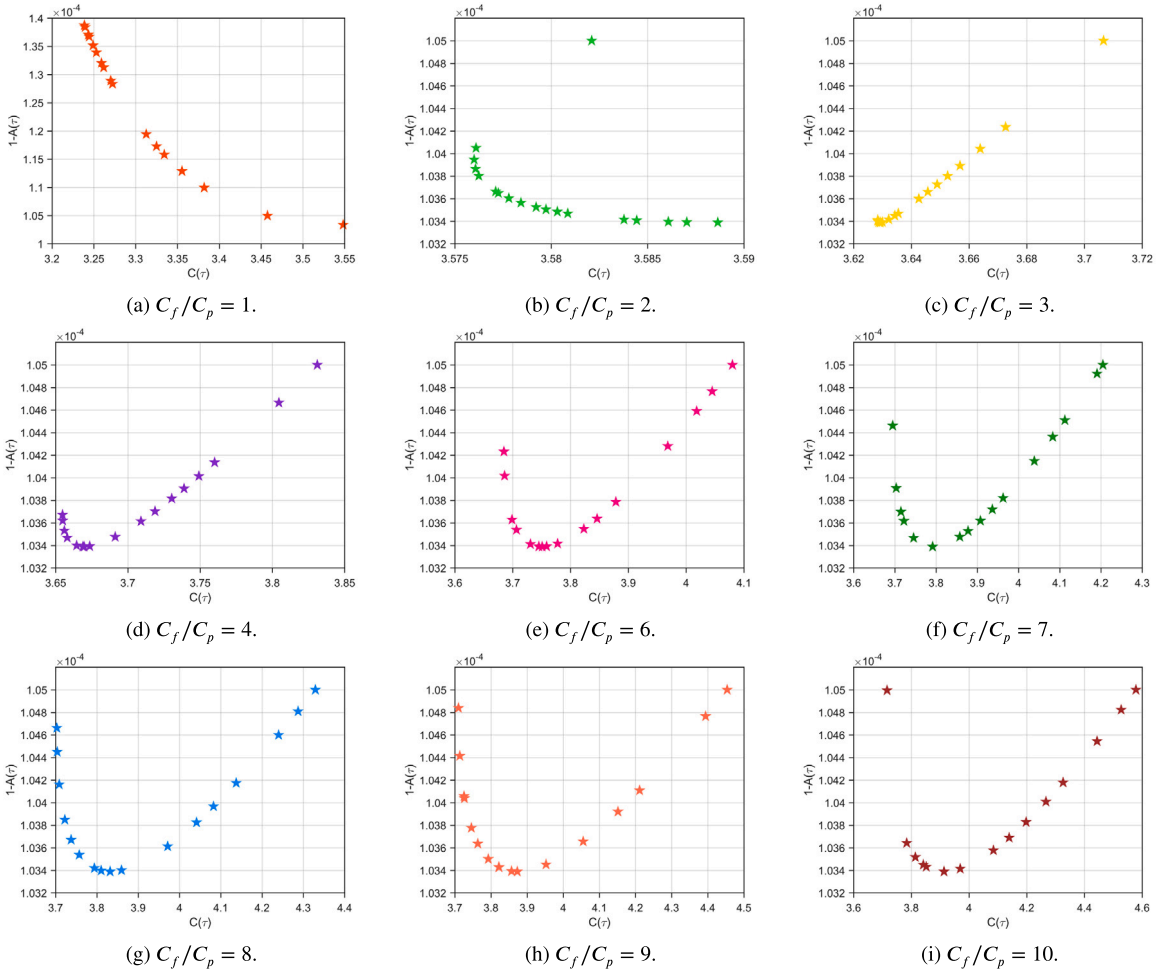

(a) $C_f/C_p = 1$. (b) $C_f/C_p = 2$. (c) $C_f/C_p = 3$.

(d) $C_f/C_p = 4$. (e) $C_f/C_p = 6$. (f) $C_f/C_p = 7$.

(g) $C_f/C_p = 8$. (h) $C_f/C_p = 9$. (i) $C_f/C_p = 10$.

Fig. 30. Two-dimensional Pareto frontiers of $C(\tau)$ and $\overline{A}(\tau)$ in different C_f/C_p for B0006.

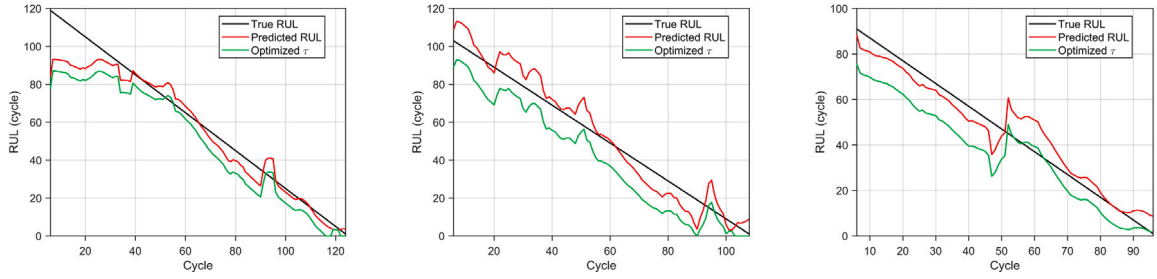

(a) The τ^* of B0005. (b) The τ^* of B0006. (c) The τ^* of B0018.

Fig. 31. The τ^* of different batteries in various prediction starting time in Case study 2.

probabilistic RUL predictions compared to both CNN- or RNN-based models and MA-TCN-QLOSS models.

Based on the RUL PDF, we proposed an opportunistic maintenance strategy for lithium-ion batteries. For single-component maintenance decisions, we balanced maintenance costs, component availability and reliability measures to achieve multi-objective maintenance optimization. Using the Euclidean distance, the optimal preventive replacement time for individual batteries was determined among the solutions on the Pareto front of the multi-objective maintenance optimization problem. Experimental results indicate that the suggested replacement times occur prior to the actual failure times of the components, demonstrating the effectiveness of the proposed single-component maintenance strategy in preventing equipment failures. Furthermore, using the OM time windows, we identified the OM grouping structure for multiple lithium-ion batteries, further reducing maintenance costs.

In future research, as more maintenance information becomes available, our goal is to integrate rolling horizon optimization with predictive opportunistic maintenance, enabling both long-term maintenance planning and short-term, dynamic maintenance decision-making.

CRediT authorship contribution statement

Zongyao Wang: Visualization, Validation, Writing – original draft, Software, Methodology. **Wei Shangguan:** Supervision, Writing – review & editing, Investigation, Funding acquisition. **Zhiqiang Xu:** Software, Methodology, Investigation. **Cong Peng:** Writing – review & editing, Validation, Methodology. **Enrico Zio:** Supervision, Investigation, Writing – review & editing. **Baigen Cai:** Writing – review & editing, Supervision.

Declaration of competing interest

The authors declare that there are no conflicts of interest regarding the publication of this paper.

Acknowledgments

The authors thankfully acknowledge the financial support provide by the Fundamental Research Funds for the Central Universities, China 2024YJS115, the Beijing Natural Science Foundation Fengtai Rail Transit Frontier Research Joint Fund under Grant L231003, the National Nature Science Foundation of China Projects under Grant 52272328, and the Equipment Preresearch Joint Foundation of Ministry of Education under Grant 8091B022238. Moreover, we would like to thank the editors, the Associate Editor, and three reviewers for their help in improving the quality of the paper.

Data availability

The authors do not have permission to share data.

References

[1] K. Gao, Z. Huang, C. Lyu, C. Liu, Multi-scale prediction of remaining useful life of lithium-ion batteries based on variational mode decomposition and integrated machine learning, J. Energy Storage 99 (2024) 113372.
[2] R. Wang, M. Zhu, X. Zhang, Lifetime prediction and maintenance assessment of lithium-ion batteries based on combined information of discharge voltage curves and capacity fade, J. Energy Storage 81 (2024) 110376.
[3] G. Pozzato, A. Allam, S. Onori, Lithium-ion battery aging dataset based on electric vehicle real-driving profiles, Data Brief 41 (2022) 107995.
[4] A. Ruvio, O. Bayrak, A preliminary design of a hybrid train's on-board batteries for a 25 kV–50 Hz high speed railway line, J. Energy Storage 84 (2024) 110966.
[5] N. Ghaviha, J. Campillo, M. Bohlin, E. Dahlquist, Review of application of energy storage devices in railway transportation, Energy Procedia 105 (2017) 4561–4568.
[6] A. Manthiram, An outlook on lithium ion battery technology, ACS Cent. Sci. 3 (10) (2017) 1063–1069.
[7] J. Ma, B. Chen, L. Wang, G. Cui, Progress and prospect on failure mechanisms of solid-state lithium batteries, J. Power Sources 392 (2018) 94–115.
[8] I. de Pater, A. Reijns, M. Mitici, Alarm-based predictive maintenance scheduling for aircraft engines with imperfect remaining useful life prognostics, Reliab. Eng. Syst. Saf. 221 (2022) 108341.
[9] M. Mitici, I. de Pater, A. Barros, Z. Zeng, Dynamic predictive maintenance for multiple components using data-driven probabilistic RUL prognostics: The case of turbofan engines, Reliab. Eng. Syst. Saf. 234 (2023) 109199.
[10] J. Lee, M. Mitici, Deep reinforcement learning for predictive aircraft maintenance using probabilistic remaining-useful-life prognostics, Reliab. Eng. Syst. Saf. 230 (2023) 108908.
[11] K. Li, N. Xie, H. Li, A hybrid grey approach for battery remaining useful life prediction considering capacity regeneration, Expert Syst. Appl. (2025) 126905.
[12] J. Li, M. Ye, Y. Wang, Q. Wang, M. Wei, A hybrid framework for predicting the remaining useful life of battery using Gaussian process regression, J. Energy Storage 66 (2023) 107513.
[13] Z. Xu, Y. Zhang, Q. Miao, An attention-based multi-scale temporal convolutional network for remaining useful life prediction, Reliab. Eng. Syst. Saf. (2024) 110288.
[14] Z. Jia, Z. Li, K. Zhao, K. Wang, S. Wang, Z. Liu, CNN-DBLSTM: A long-term remaining life prediction framework for lithium-ion battery with small number of samples, J. Energy Storage 97 (2024) 112947.
[15] Q. Xie, R. Liu, J. Huang, J. Su, Residual life prediction of lithium-ion batteries based on data preprocessing and a priori knowledge-assisted CNN-LSTM, Energy 281 (2023) 128232.
[16] F. Guo, X. Wu, L. Liu, J. Ye, T. Wang, L. Fu, Y. Wu, Prediction of remaining useful life and state of health of lithium batteries based on time series feature and Savitzky–Golay filter combined with gated recurrent unit neural network, Energy 270 (2023) 126880.
[17] P. Liang, Z. Yu, B. Wang, X. Xu, J. Tian, Fault transfer diagnosis of rolling bearings across multiple working conditions via subdomain adaptation and improved vision transformer network, Adv. Eng. Inform. 57 (2023) 102075.
[18] C. Chen, G. Tao, J. Shi, M. Shen, Z.H. Zhu, A lithium-ion battery degradation prediction model with uncertainty quantification for its predictive maintenance, IEEE Trans. Ind. Electron. 71 (4) (2023) 3650–3659.
[19] C. Chen, J. Shi, M. Shen, L. Feng, G. Tao, A predictive maintenance strategy using deep learning quantile regression and kernel density estimation for failure prediction, IEEE Trans. Instrum. Meas. 72 (2023) 1–12.
[20] Z. Wang, W. Shangguan, C. Peng, Y. Meng, L. Chai, B. Cai, A predictive maintenance strategy for a single device based on remaining useful life prediction information: A case study on railway gyroscope, IEEE Trans. Instrum. Meas. (2024).
[21] D. Jarčević, L. Radovanović, J. Pekez, B. Novaković, H. Glavaš, The influence of preventive maintenance of batteries on increasing the security of the thermal power system, in: International Conference on Organization and Technology of Maintenance, Springer, 2022, pp. 96–105.
[22] Q. Wu, Q. Feng, Y. Ren, Q. Xia, Z. Wang, B. Cai, An intelligent preventive maintenance method based on reinforcement learning for battery energy storage systems, IEEE Trans. Ind. Inform. 17 (12) (2021) 8254–8264.
[23] C. Peng, W. Shangguan, J. Peng, Z. Wang, L. Chai, B. Cai, Y. Xing, Multi-objective preventive maintenance strategy and optimization considering unavailability and cost: A case study on VOBC, Alex. Eng. J. 105 (2024) 567–577.
[24] Y. Yang, A machine-learning prediction method of lithium-ion battery life based on charge process for different applications, Appl. Energy 292 (2021) 116897.
[25] B. Chen, Y. Liu, B. Xiao, A novel hybrid neural network-based SOH and RUL estimation method for lithium-ion batteries, J. Energy Storage 98 (2024) 113074.
[26] A. Vaswani, N. Shazeer, N. Parmar, J. Uszkoreit, L. Jones, A.N. Gomez, Ł. Kaiser, I. Polosukhin, Attention is all you need, Adv. Neural Inf. Process. Syst. 30 (2017).
[27] T. Pan, J. Chen, Z. Ye, A. Li, A multi-head attention network with adaptive meta-transfer learning for RUL prediction of rocket engines, Reliab. Eng. Syst. Saf. 225 (2022) 108610.
[28] Y. Ge, J. Ma, G. Sun, A structural pruning method for lithium-ion batteries remaining useful life prediction model with multi-head attention mechanism, J. Energy Storage 86 (2024) 111396.
[29] G. Wang, L. Sun, A. Wang, J. Jiao, J. Xie, Lithium battery remaining useful life prediction using VMD fusion with attention mechanism and TCN, J. Energy Storage 93 (2024) 112330.
[30] S. Bai, J.Z. Kolter, V. Koltun, An empirical evaluation of generic convolutional and recurrent networks for sequence modeling, 2018, arXiv preprint arXiv: 1803.01271.
[31] Y. Cao, Y. Ding, M. Jia, R. Tian, A novel temporal convolutional network with residual self-attention mechanism for remaining useful life prediction of rolling bearings, Reliab. Eng. Syst. Saf. 215 (2021) 107813.
[32] F. Deng, Y. Bi, Y. Liu, S. Yang, Remaining useful life prediction of machinery: A new multiscale temporal convolutional network framework, IEEE Trans. Instrum. Meas. 71 (2022) 1–13.
[33] A. Amini, W. Schwarting, A. Soleimany, D. Rus, Deep evidential regression, Adv. Neural Inf. Process. Syst. 33 (2020) 14927–14937.
[34] M. Sensoy, L. Kaplan, M. Kandemir, Evidential deep learning to quantify classification uncertainty, Adv. Neural Inf. Process. Syst. 31 (2018).

[35] A. Malinin, M. Gales, Predictive uncertainty estimation via prior networks, Adv. Neural Inf. Process. Syst. 31 (2018).
[36] B. Wang, Y. Lei, N. Li, N. Li, A hybrid prognostics approach for estimating remaining useful life of rolling element bearings, IEEE Trans. Reliab. 69 (1) (2018) 401–412.
[37] X. Fang, K. Paynabar, N. Gebraeel, Multistream sensor fusion-based prognostics model for systems with single failure modes, Reliab. Eng. Syst. Saf. 159 (2017) 322–331.
[38] R. He, Z. Tian, M.J. Zuo, A semi-supervised GAN method for RUL prediction using failure and suspension histories, Mech. Syst. Signal Process. 168 (2022) 108657.
[39] A. Kendall, Y. Gal, What uncertainties do we need in bayesian deep learning for computer vision? Adv. Neural Inf. Process. Syst. 30 (2017).
[40] B.W. Silverman, Density Estimation for Statistics and Data Analysis, Routledge, 2018.
[41] R. Jiang, P. Ji, Age replacement policy: a multi-attribute value model, Reliab. Eng. Syst. Saf. 76 (3) (2002) 311–318.
[42] H. Shi, J. Zeng, Real-time prediction of remaining useful life and preventive opportunistic maintenance strategy for multi-component systems considering stochastic dependence, Comput. Ind. Eng. 93 (2016) 192–204.
[43] C. Birkl, Diagnosis and Prognosis of Degradation in Lithium-Ion Batteries (Ph.D. thesis), University of Oxford, 2017.
[44] C. Birkl, Oxford battery degradation dataset 1, 2017.
[45] B. Saha, K. Goebel, Battery data set, NASA AMES Progn. Data Repos. (2007).
[46] F. Xia, Y. Yu, J. Chen, SOH and RUL prediction of lithium batteries based on fusions of RLOESS filtered electrochemical and thermal features by bidirectional gated recurrent unit network, J. Energy Storage 102 (2024) 114134.
[47] I. Jorge, T. Mesbahi, A. Samet, R. Boné, Time series feature extraction for lithium-ion batteries state-of-health prediction, J. Energy Storage 59 (2023) 106436.
[48] G. Ma, Y. Zhang, C. Cheng, B. Zhou, P. Hu, Y. Yuan, Remaining useful life prediction of lithium-ion batteries based on false nearest neighbors and a hybrid neural network, Appl. Energy 253 (2019) 113626.
[49] L. Ren, J. Dong, X. Wang, Z. Meng, L. Zhao, M.J. Deen, A data-driven auto-CNN-LSTM prediction model for lithium-ion battery remaining useful life, IEEE Trans. Ind. Inform. 17 (5) (2020) 3478–3487.
[50] J. Hong, Y. Chen, Q. Chai, Q. Lin, W. Wang, State-of-health estimation of lithium-ion batteries using a novel dual-stage attention mechanism based recurrent neural network, J. Energy Storage 72 (2023) 109297.
[51] D. Chen, W. Hong, X. Zhou, Transformer network for remaining useful life prediction of lithium-ion batteries, IEEE Access 10 (2022) 19621–19628.
[52] T. Fischer, M. Sterling, S. Lessmann, Fx-spot predictions with state-of-the-art transformer and time embeddings, Expert Syst. Appl. 249 (2024) 123538.
[53] Y. Qin, D. Song, H. Chen, W. Cheng, G. Jiang, G. Cottrell, A dual-stage attention-based recurrent neural network for time series prediction, 2017, arXiv preprint arXiv:1704.02971.
[54] S. Mao, X. Li, B. Zhao, Remaining useful life prediction based on time-series features and conformalized quantile regression, Meas. Sci. Technol. 35 (12) (2024) 126113.
[55] Y. Ji, Z. Chen, Y. Shen, K. Yang, Y. Wang, J. Cui, An RUL prediction approach for lithium-ion battery based on SADE-MESN, Appl. Soft Comput. 104 (2021) 107195.
[56] D. Yang, X. Zhang, R. Pan, Y. Wang, Z. Chen, A novel Gaussian process regression model for state-of-health estimation of lithium-ion battery using charging curve, J. Power Sources 384 (2018) 387–395.